



TEZ ŞABLONU ONAY FORMU
THESIS TEMPLATE CONFIRMATION FORM

1. Şablonda verilen yerleşim ve boşluklar değiştirilmemelidir.
2. **Jüri tarihi** Başlık Sayfası, İmza Sayfası, Abstract ve Öz'de ilgili yerlere yazılmalıdır.
3. İmza sayfasında jüri üyelerinin unvanları doğru olarak yazılmalıdır. Tüm imzalar **mavi pilot kalemle** atılmalıdır.
4. **Disiplinlerarası** programlarda görevlendirilen öğretim üyeleri için jüri üyeleri kısmında tam zamanlı olarak çalıştıkları anabilim dalı başkanlığının ismi yazılmalıdır. Örneğin: bir öğretim üyesi Biyoteknoloji programında görev yapıyor ve biyoloji bölümünde tam zamanlı çalışıyorsa, İmza sayfasına biyoloji bölümü yazılmalıdır. İstisnai olarak, disiplinler arası program başkanı ve tez danışmanı için disiplinlerarası program adı yazılmalıdır.
5. Tezin **son sayfasının sayfa** numarası Abstract ve Öz'de ilgili yerlere yazılmalıdır.
6. Bütün chapterlar, referanslar, ekler ve CV sağ sayfada başlamalıdır. Bunun için **kesmeler** kullanılmıştır. **Kesmelerin kayması** fazladan boş sayfaların oluşmasına sebep olabilir. Bu gibi durumlarda paragraf (¶) işaretine tıklayarak kesmeleri görünür hale getirin ve yerlerini **kontrol edin**.
7. Figürler ve tablolar kenar boşluklarına taşmamalıdır.
8. Şablonda yorum olarak eklenen uyarılar dikkatle okunmalı ve uygulanmalıdır.
9. Tez yazdırılmadan önce PDF olarak kaydedilmelidir. Şablonda yorum olarak eklenen uyarılar PDF dokümanında yer almamalıdır.
10. **Bu form aracılığıyla oluşturulan PDF dosyası arkalı-önlü baskı alınarak tek bir spiralli cilt haline getirilmelidir.**
11. Spiralli hale getirilen tez taslağınızdaki ilgili alanları imzalandıktan sonra, [Tez Jüri Atama Formu](#) ile birlikte bölüm sekreterliğine teslim edilmelidir.
12. Tez taslaklarının kontrol işlemleri tamamlandığında, bu durum öğrencilere METU uzantılı öğrenci e-posta adresleri aracılığıyla duyurulacaktır.
13. Tez yazım süreci ile ilgili herhangi bir sıkıntı yaşarsanız, [Sıkça Sorulan Sorular \(SSS\)](#) sayfamızı ziyaret ederek yaşadığınız sıkıntıyla ilgili bir çözüm bulabilirsiniz.

1. Do not change the spacing and placement in the template.
2. Write **defense date** to the related places given on Title page, Approval page, Abstract and Öz.
3. Write the titles of the examining committee members correctly on Approval Page. **Blue ink** must be used for all signatures.
4. For faculty members working in **interdisciplinary programs**, the name of the department that they work full-time should be written on the Approval page. For example, if a faculty member staffs in the biotechnology program and works full-time in the biology department, the department of biology should be written on the approval page. Exceptionally, for the interdisciplinary program chair and your thesis supervisor, the interdisciplinary program name should be written.
5. Write **the page number of the last page** in the related places given on Abstract and Öz pages.
6. All chapters, references, appendices and CV must be started on the right page. **Section Breaks** were used for this. **Change in the placement** of section breaks can result in extra blank pages. In such cases, make the section breaks visible by clicking paragraph (¶) mark and **check their position**.
7. All figures and tables must be given inside the page. Nothing must appear in the margins.
8. All the warnings given on the comments section through the thesis template must be read and applied.
9. Save your thesis as pdf and Disable all the comments before taking the printout.
10. **Print two-sided the PDF file that you have created through this form and make a single spiral bound.**
11. Once you have signed the relevant fields in your thesis draft that you spiraled, submit it to the department secretary together with your [Thesis Jury Assignment Form](#).
12. This will be announced to the students via their METU students e-mail addresses when the control of the thesis drafts has been completed.
13. If you have any problems with the thesis writing process, you may visit our [Frequently Asked Questions \(FAQ\)](#) page and find a solution to your problem.

Yukarıda bulunan tüm maddeleri okudum, anladım ve kabul ediyorum. / I have read, understand and accept all of the items above.

Name : Sencer
Surname : Aydın
E-Mail : e232279@metu.edu.tr
Date : 29.07.2021
Signature : _____

**EFFECT OF ANNEALING ON THE MECHANICAL PROPERTIES OF
PLA PARTS PRODUCED BY FUSED FILAMENT FABRICATION**

A THESIS SUBMITTED TO
THE GRADUATE SCHOOL OF NATURAL AND APPLIED SCIENCES
OF
MIDDLE EAST TECHNICAL UNIVERSITY

BY

SENCER AYDIN

IN PARTIAL FULFILLMENT OF THE REQUIREMENTS
FOR
THE DEGREE OF MASTER OF SCIENCE
IN
MICRO AND NANOTECHNOLOGY

SEPTEMBER 2021

Approval of the thesis:

**MECHANICAL PROPERTIES OF PLA PARTS PRODUCED BY FUSED
FILAMENT FABRICATION**

submitted by **SENCER AYDIN** in partial fulfilment of the requirements for the degree of **Master of Science in Micro and Nanotechnology, Middle East Technical University** by,

Prof. Dr. Halil Kalıpçılar
Dean, Graduate School of **Natural and Applied Sciences** _____

Prof. Dr. Almıla Güvenç Yazıcıoğlu
Head of the Department, **Micro and Nanotechnology** _____

Assoc. Prof. Dr. Sezer Özerinç
Supervisor, **Micro and Nanotechnology, METU** _____

Examining Committee Members:

Assoc. Prof. Dr. Mehmet Bülent Özer
Mechanical Engineering, METU _____

Assoc. Prof. Dr. Sezer Özerinç
Micro and Nanotechnology, METU _____

Assoc. Prof. Dr. Ulaş Yaman
Mechanical Engineering, METU _____

Assoc. Prof. Dr. Erhan Bat
Chemical Engineering, METU _____

Asst. Prof. Dr. Recep Muhammet Görgülüarslan
Mechanical Engineering, TOBB ETU _____

Date: 09.01.2021

I hereby declare that all information in this document has been obtained and presented in accordance with academic rules and ethical conduct. I also declare that, as required by these rules and conduct, I have fully cited and referenced all material and results that are not original to this work.

Name Last name : Aydın, Sencer

Signature :

ABSTRACT

EFFECT OF ANNEALING ON THE MECHANICAL PROPERTIES OF PLA PARTS PRODUCED BY FUSED FILAMENT FABRICATION

Aydın, Sencer
Master of Science, Micro and Nanotechnology
Supervisor : Assoc. Prof. Dr. Sezer Özerinç

August 2021, 79 pages

Additive manufacturing has become a disruptive technology for the production of load bearing components in a wide range of applications. Fused filament fabrication (FFF) is among the most effective and economical techniques for the printing of polymeric parts. There are numerous thermoplastic materials suitable for FFF. Among these, Polylactic acid (PLA) is a renewable, sustainable and cost-effective alternative. For better utilization of PLA parts produced by FFF, there is a need to understand the structure-property relationships in this system. This thesis investigated the effect of annealing on the mechanical properties of FFF produced parts made of polylactic acid (PLA). The as-printed specimens exhibit an amorphous structure, whereas annealing at elevated temperatures, ranging from 80°C to 140°C for 24 hours resulted in the formation of different crystalline phases. 100°C annealing for 24 hours provided the best results in terms of ductility and strength improvement; the tensile strength increased by 6.5 % and elongation at break increased by 33%. A further increase in the annealing temperature resulted in a decrease in the strength and ductility. In the second part of the thesis, the effect of annealing for different infill ratios were investigated. The 60% infill ratio case with

100 °C annealing showed the best normalized mechanical properties. The findings of the thesis show the importance of the microstructure on the mechanical properties and demonstrate the feasibility of annealing for the process and property optimization of FFF-produced parts.

Keywords: additive manufacturing, fused filament fabrication, polylactic acid (PLA), annealing, mechanical properties, crystallization

ÖZ

ISIL İŞLEMİN ERİYİK FİLAMANT İLE İMALAT YÖNTEMİYLE ÜRETİLMİŞ PLA PARÇALARIN MEKANİK ÖZELLİKLERİNE ETKİSİNİN İNCELENMESİ

Aydın, Sencer
Master of Science, Micro and Nanotechnology
Supervisor: Assoc. Prof. Dr. Sezer Özerinç

Ağustos 2021, 79 sayfa

Eklemeli imalat, mühendislik sistemlerinde yük taşıyan bileşenlerin üretimi için uygulanabilir bir teknoloji haline gelmiştir. Bu kapsamda, Eriyik Filament ile İmalat (EFİ), polimerik parçaların baskısı için en etkili ve ekonomik yöntemler arasındadır. EFİ yöntemine uygun çok sayıda termoplastik malzeme mevcuttur. Bunlar arasında Polilaktik asit (PLA), yenilenebilir, sürdürülebilir ve düşük maliyetli bir alternatif olarak öne çıkmaktadır. EFİ ile üretilen PLA yapıların uygulamalarda daha etkili şekilde kullanılabilmesi için ilgili proses-yapı-özellik ilişkilerinin anlaşılmasına ihtiyaç vardır. Bu tez çalışması, ısıl işlem uygulamasının EFİ ile üretilmiş PLA parçaların mekanik özellikleri üzerindeki etkisini araştırmıştır. Basılan numuneler amorf bir yapı sergilerken, 24 saat boyunca 80°C ile 140°C arasında değişen sıcaklıklarda uygulanan ısıl işlem, farklı kristal fazların oluşmasına neden olmuştur. 100°C'de uygulanan ısıl işlem, dayanım ve süneklik iyileştirmesi açısından en iyi sonuçları vermiş; bu kapsamda çekme dayanımı %6.5, kopma uzaması ise %33 artmıştır. Daha yüksek sıcaklıklarda ise mekanik özelliklerde düşüş yaşanmıştır. Farklı dolgu oranları incelendiğinde, %60 dolgu baskısı ve 100°C'deki ısıl işlemin en yüksek özgül dayanımı sağladığı tespit

edilmiştir. Sonuçlar, ısıtım işlem yönteminin EFi tekniđiyle üretilen parçalarda mekanik özellikleri iyileştirmek için etkili bir yöntem olduğunu ortaya koymuştur.

Anahtar Kelimeler: eklemeli imalat, eriyik filament ile imalat, polilaktik asit (PLA), ısıtım işlem, mekanik özellikler, kristalleşme

Dedicated to my family

ACKNOWLEDGMENTS

This thesis would be not possible without the support of many people in my life. It was quite an enjoyable and memorable experience that I worked with nice and intelligent people. Thus, I take this chance to acknowledge each of them who have helped and supported me to this study.

I would like to express my gratitude to my supervisor, Assoc. Prof. Dr. Sezer Özerinç and my co-worker Servet Şehirli for their guidance, advice, support, encouragement and valuable suggestions throughout the course of the studies and experimentation.

Thanks are to all my friends in Nanomechanics Laboratory at the Department of Mechanical Engineering, METU, especially, Can Okuyucu for their endless support in the completion of the thesis.

Finally, I would like to thank my family members for their endless support, encouragement, motivation, and advices.

TABLE OF CONTENTS

ABSTRACT.....	v
ÖZ.....	vii
ACKNOWLEDGMENTS	x
TABLE OF CONTENTS.....	xi
LIST OF TABLES	xiii
LIST OF FIGURES	xiv
1 INTRODUCTION	1
1.1 Fused Filament Fabrication.....	3
1.2 Polylactide (Polylactic Acid).....	5
1.3 Extrinsic and Intrinsic Properties of Additively Manufactured Specimens	8
1.3.1 Extrinsic Properties	8
1.3.2 Intrinsic Properties	9
2 EXPERIMENTAL PROCEDURES.....	15
2.1 Specimen Production.....	15
2.2 Annealing	18
2.3 Mechanical Characterization.....	20
2.4 Structural Characterization.....	20
2.4.1 Microstructural Characterization	20

2.4.2	X-Ray Diffraction (XRD)	21
2.4.3	Differential Scanning Calorimetry (DSC)	23
3	RESULTS AND DISCUSSION	25
3.1	XRD Analysis	25
3.1.1	Crystallite Size Prediction.....	31
3.2	DSC Analysis	33
3.3	Comparison of XRD and DSC Results	38
3.4	Effect of Annealing on Crystallinity Level	40
3.5	Mechanical Properties	44
3.5.1	Mechanical Properties of Temperature Controlled Specimens.....	45
3.5.2	Mechanical Properties of Infill Controlled Specimens	50
3.6	Micrographic Examinations	55
3.6.1	Micrographic Examinations of Temperature Controlled Specimens	55
3.6.2	Micrographic Examinations of Infill Controlled Specimens	57
4	CONCLUSION AND FUTURE WORK	65
4.1	Future Work	68
5	REFERENCES	71

LIST OF TABLES

TABLES

Table 2.1. Printing parameters.	16
Table 2.2. A summary of specimens prepared and their naming convention.	19
Table 3.1. Diffraction data obtained from diffraction database, Central Laboratories, METU (Brizzolara et al., 1996).	26
Table 3.2. Raw diffraction data of 140 °C specimen. 2 Theta angle values are at leftmost column, and d values are given in angstrom. Peak centers are given at third column and rightmost column is holding the values of percentage area of peaks compared to the major peak.	27
Table 3.3. Melting enthalpy (ΔH_m), cold crystallization enthalpy (ΔH_c) and melting point (T_m) comparison between specimens	36

LIST OF FIGURES

FIGURES

Figure 1.1. SLS printer and its product (left) (Sinterit, 2021), DLP printer and its product (right) (Gurrapu, 2020).	2
Figure 1.2. Schematic of traditional FFF printer design and working principle. 1 shows the nozzle which pushes the molten filament with given radius. 2 shows the base plate which allows the filament to be stuck on the surface and controls Z direction of printing. 3 shows the axial motion of the nozzle, giving the X-Y axis of printing. (Almeida, 2020).....	4
Figure 1.3. Conversion of lactic acid to polylactic acid. The polymer chain length is denoted with n (Mckeen, 2012).	5
Figure 1.4. L and D configurations of polylactide monomers (lactic acid) (Rebelo et al., 2016).	6
Figure 1.5. Commercial stents: (a) Igaki-Tamai stent® (b) Absorb stent®, (c) Amaranth stent® (d) Stent DESolve ® (Rebelo et al., 2016).....	7
Figure 1.6. Comparison between SiO ₂ (left) and polymer structure (right) (Booth et al., 2017).	10
Figure 2.1. (a) Geometry of the ASTM 638 Type 5 tensile test specimen. Dimensions are in mm. Sample thickness is 3 mm. (b) A schematic showing the printing and raster orientation with respect to the extrusion axis. The given schematic is also valid for the first group specimens.	15
Figure 2.2. Images of sliced test specimens with different infill ratios.	17
Figure 2.3. Sliced specimen with %50 infill ratio. The red circles show the welded regions between the headpieces and neck region.	17
Figure 2.4. Raw XRD graph of PET sample, showing the machine background (noise), amorphous halo and crystalline peaks (Lamba, 2016).....	22
Figure 2.5. DSC scan of polyetheretherketone. Note that crystallization peak noted is cold crystallization peak (Intertek, 2021).....	23
Figure 3.1. (a) XRD data of as printed and annealed specimens. (b) Close-up view of the (200) and (014) peaks.	29

Figure 3.2. Separate XRD graph driven by raw diffraction data collected from SR sample group. Amorphous diffraction can be easily noticed.....	30
Figure 3.3. (a) (014), (b) (200) and (c) (104) Miller indices interplanar spacing data for S80 to S140 specimens.....	31
Figure 3.4. Sample groups and calculated a (a), b (b), c (c) and cell volume (d) values for the orthorhombic cell of PLA crystals.	33
Figure 3.5. DSC scan under nitrogen purge conditions, with 10 C/min heating/cooling rate. The red arrow shows the melting behaviour and black arrow shows the pre-melting endotherm.	34
Figure 3.6. DSC scan for the specimens, zoomed in near their melting temperature to indicate the melting points and endotherm peaks. Melting points are shown with red circle and endotherm peaks are shown with black circle. Endo flow is upwards and the curves are fit above each other for easier comparison. Y axis does not show the absolute values.	35
Figure 3.7. DSC scan from literature data. Annealing temperatures and hours can be denoted at left and crystalline structures at right of the thermal graph. Endo flow is downwards. (Tabi et al., 2016).....	36
Figure 3.8. XRD and DSC crystallinity ratio comparison. The crystallinity data is fit to a curve, with a third-degree polynomial. Note the distinctive jump at 120 C°.	39
Figure 3.9. Lauritzen-Hoffman plot for nucleation density and growth rate. Red dots and lines show the growth rate and black dots, and lines show the nucleation density. The scattered red lines represent α' phase and full red lines represents α phase plot. Note the increased crystal growth rate as temperature rises. (Foglia et al. 2020).	42
Figure 3.10. Ultimate tensile stress and strain (a), resilience unit (b), and tensile modulus (c) results. The values are average values of the tested specimens.....	46
Figure 3.11. Annealing temperature versus tensile strength and modulus (Tabi et al., 2016).	49

Figure 3.12. The stress-strain graphs of all specimen groups. Note that the given result is for one specimen in each group.....	49
Figure 3.13. Force versus infill ratio graph. Deviations in the test groups can be seen by the bars. Variations between heat treated and untreated specimens are shown. Suffix of A denotes annealing and I denotes infill percentage.....	50
Figure 3.14. Force per layer versus infill graph. Deviations in the test groups can be seen by the bars. Variations between heat treated and untreated specimens are shown. Suffix of A denotes annealing and I denotes infill percentage.....	51
Figure 3.15. Strain versus infill graph. Suffix of A denotes annealing and I denotes infill percentage.....	52
Figure 3.16. Resilience versus infill graph. Suffix of A denotes annealing and I denotes infill percentage.	53
Figure 3.17. Resilience per layer versus infill graph. Suffix of A denotes annealing and I denotes infill percentage.	54
Figure 3.18. SEM pictures of SR specimens. Left picture shows the shell part, and right picture shows the raster part. Note the defects of the shell part, and the gaps shown by yellow circles.....	55
Figure 3.19. SEM pictures of S80 specimens. Left picture shows the shell part and its defects, and right picture shows the raster and shell part combined. Note the defects of the shell part, and the gaps shown by yellow circles.....	56
Figure 3.20. SEM pictures of S120 specimens. Left picture shows the shell part and its defects, and right picture shows the raster part. Note the defects and the gaps shown by yellow circles.....	56
Figure 3.21. Micrographs of 50 percent infill printed specimen. Left micrograph shows 40x and right micrograph shows 100x magnification. The micrograph is taken from the fracture site.	57
Figure 3.22. Micrographs of 60 percent infill printed specimen. Left micrograph shows 40x and right micrograph shows 100x magnification. The micrograph is taken from the fracture site.	58

Figure 3.23. Micrographs of 60 percent infill printed heat treated specimen. Left micrograph shows 40x and right micrograph shows 100x magnification. The micrograph is taken from the fracture site. 58

Figure 3.24. Micrographs of 70 percent infill printed specimen. Left micrograph shows 40x and right micrograph shows 100x magnification. The micrograph is taken from the fracture site. 59

Figure 3.25. Micrographs of 70 percent infill printed heat treated specimen. Left micrograph shows 40x and right micrograph shows 100x magnification. The micrograph is taken from the fracture site. 60

Figure 3.26. Micrographs of 80 percent infill printed specimen. Left micrograph shows 40x and right micrograph shows 100x magnification. The micrograph is taken from the fracture site. 60

Figure 3.27. Micrographs of 80 percent infill printed heat treated specimen. Left micrograph shows 40x and right micrograph shows 100x magnification. The micrograph is taken from the fracture site. 61

Figure 3.28. Micrographs of 90 percent infill printed specimen. Left micrograph shows 40x and right micrograph shows 100x magnification. The micrograph is taken from the fracture site. 61

Figure 3.29. Micrographs of 90 percent infill printed heat treated specimen. Left micrograph shows 40x and right micrograph shows 100x magnification. The micrograph is taken from the fracture site. 62

Figure 3.30. Micrographs of 100 percent infill printed specimen. Left micrograph shows 40x and right micrograph shows 100x magnification. The micrograph is taken from the fracture site. 63

Figure 3.31. Micrographs of 100 percent infill printed heat treated specimen. Left micrograph shows 40x and right micrograph shows 100x magnification. The micrograph is taken from the fracture site. 63

CHAPTER 1

INTRODUCTION

Additive Manufacturing (AM) technology is an advanced manufacturing technique used to manufacture a part layer by layer from a computer-aided design (CAD) file. In the process, the object is built by adding material layers to create the designed part. The layered fabrication scheme of AM enables the user to finalize production without having to purchase expensive production tools and apparatus.

Additive manufacturing enables the user to produce either the final product or a prototype for the final product. Additive manufacturing has a very broad selection of production types, yet all have the one common property, which gives the advantage of defining details: layer by layer production. Layer by layer production, albeit more expensive and harder to control than conventional production methods, gives the user the advantage of the ability to define outer and inner features, heterogenous production. Conventional methods, like extrusion and moulding on polymers or forging and casting on metals, would mean the product would be largely homogenous; formation of intentional voids, different infill ratios inside the material, production of micro features or using different materials at same time, without using additional joining methods (welding, soldering, etc.) is hardly doable. Additive manufacturing, however, enables the possibility of heterogenous production and formation of inner features.

However, additive manufacturing has a distinct disadvantage, when serial and large batch of production is needed. Printing times are higher than conventional production types, as the production is limited by one material at same time, while the conventional production types like extrusion, would enable a high production

rate with multiple products produced in one step. Even if the recent developments on printers and printing materials shortened the time for printing procedures, it is still not comparable with the well-established production times of the conventional production times.

It does not mean that additive manufacturing is not used in industry or daily applications in our life. The ability to create micro features, with strict tolerances and the high customization demand on surgical or dental applications would mean additive manufactured materials are preferred over hardly customizable conventional counterparts. In addition to that, the ability to fuse different materials during production, to generate different infills over the material, is important for aircraft and automotive engineering, as joining dissimilar materials are widespread on those industries.

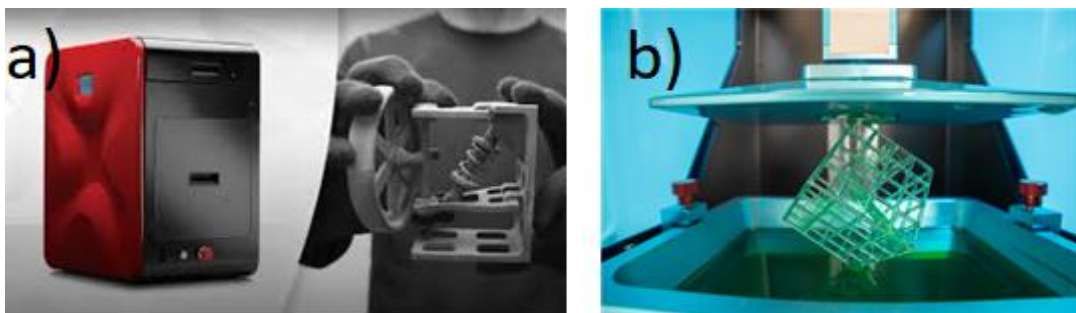


Figure 1 SLS printer and its product (left) (Sinterit, 2021), DLP printer and its product (right) (Gurrapu, 2020).

Figure 1.1. shows the examples of various printers. SLS uses laser light to sinter fine powders to create layers. DLP printers use digital projectors to cure photosensitive resin, by selectively curing the resin by employing light.

Additive manufacturing consists of a very broad spectrum of production types and material selection. From photosensitive resins to thermoplastic polymers, to metal powders, it consists of a wide spectrum of “printable” materials. There are many commercial additive manufacturing systems available in the market such as fused filament fabrication (FFF), direct metal deposition (DMD), selective laser sintering

(SLS), inkjet modeling (IJM) and stereo-lithography (SLA). These systems differ in the manner of building layers and in the types of materials that can be fabricated by these processes safely. (Mohammed et. al. 2015)

1.1 Fused Filament Fabrication

As the technology progresses, different FFF printing machines are introduced to the market, with different capabilities and different designs. However, the core principle and parts does not change. The basic principle of an FFF printer, is that a filament is either supplied from outer source or produced before printing procedure. The filament must be at the same diameter of the inlet of the nozzle and the feeder and driver of the filament branch. The filament is being pushed towards the inlet of the nozzle. As the nozzle would be heated to let the filament melt, the part of the filament, which is now molten, would be squeezed down through the nozzle gap. Depending on the size of the nozzle, feeding rate of the driver and the melting point of the material, the temperature of the nozzle is determined. The polymer squeezed down through the nozzle would crawl down towards the base and solidify shortly afterwards, due to the heat transfer from the ambient atmosphere and the touched surface. As the polymers have softening points and may exhibit softer and more ductile at higher temperatures, the touched surface and/or the ambient atmosphere can be heated up to let the polymer exhibit more elastic behaviour. The touched surface, or the base for the first layer is generally heated as producing the first layer in a solid manner is important for the incoming layers. The nozzle, which is directing the molten polymer towards the base, would motion in X-Y axis, while the base of the FFF printer is motioning at Z axis. This is applicable in traditional FFF printer design, yet some newer designs allow X-Y-Z axial capability of a nozzle movement.

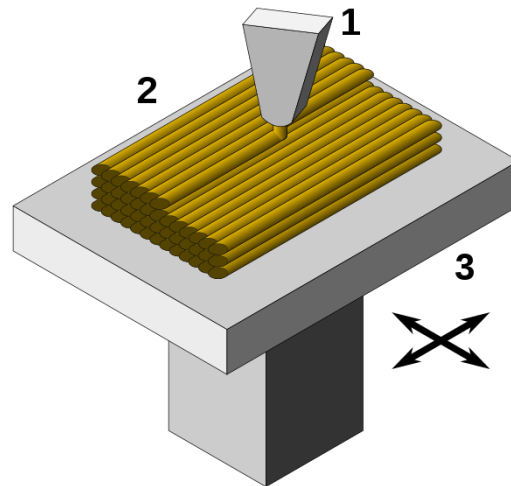


Figure 2 Schematic of traditional FFF printer design and working principle. 1 shows the nozzle which pushes the molten filament with given radius. 2 shows the base plate which allows the filament to be stuck on the surface and controls Z direction of printing. 3 shows the axial motion of the nozzle, giving the X-Y axis of printing. (Almeida, 2020).

The directions of the motions are submitted by the inner program of the FFF printer. However, to produce the CAD drawing, there should be some other software needs to be used. The CAD drawing would be first coded into XYZ coordinates of the features, then they are divided into triangular matrixes, which the FFF printer can decode and understand the features of the material. Then, the user would use the FFF printer's supplied software, to generate the drawing and to deliver the required printing parameters. Said parameters and product's CAD file would be saved then forwarded towards the printer, and the printer would decode the file and print the product according to the given parameters.

3D printers based on fused filament fabrication (FFF) technology provide a versatile and cost-effective approach to the production of custom and complex plastic parts in relatively low quantities (Wong et.al. 2012). The reasoning behind is, FFF parts can be produced with cheap materials. The electronic parts, sensors, nozzles, and mechanical parts are simple and easy to be produced. If the

components of FFF are compared to other printing methods, such as SLS which uses powerful but also fragile and expensive laser to melt or sinter the material, or DLP, which uses light to cure expensive photo resins, the production and purchase prices of FFF are considerably lower than the listed printing types.

A wide range of filament materials are suitable for FFF; some examples are polylactic acid (PLA) (Senatov et. al., 2016), acrylonitrile butadiene styrene (ABS) (Tymrak et.al., 2014) polyethylene terephthalate glycol-modified (PETG) (Alssabbagh et.al., 2017), and nylon (Tanikella et.al., 2017). The ability to control the feed of the extruding polymer, guide the nozzle and tight tolerances with acceptable reliability during printing, makes FFF an ideal candidate amongst others when it is additively manufacturing polymers. Cheaper material and printer parts makes FFF a good candidate for producing and testing large quantities of specimens.

1.2 Polylactide (Polylactic Acid)

Among these materials, polylactic acid, or polylactide (PLA) is one the most used filament materials. It has the monomer of $C_3H_4O_2$ with varying repeating units, denoted with n. The order of n holds importance as this value changes density, melting point, mechanical and chemical properties. Density ranges from 1.210 to 1.430 g/cm^3 . Melting point reported is in 150-160 °C range (Matbase, 2012).

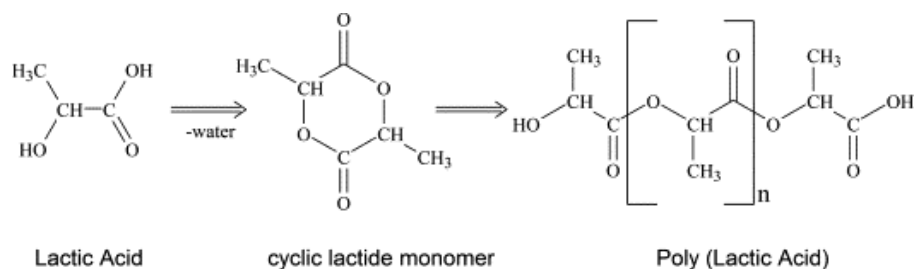


Figure 3 Conversion of lactic acid to polylactic acid. The polymer chain length is denoted with n (Mckeen, 2012).

Poly lactide is a biodegradable and renewable thermoplastic used in a wide range of applications including food packaging and medical implants (Garlotta et al., 2001). Work shows that the inclusion of poly lactide on other polymers, especially the biopolymers which are used for drug delivery systems, can be useful as it would be used as a strengthening polymer, such as PCL, to provide integrity along its polymer chains (Broz et al., 2003). In addition to these findings, another work (Farah et.al 2016) argues that poly lactide is a major component when it comes to the biodegradable materials. It can be used as pure poly lactide or used as a constituent for other biodegradable materials, like PEG or used as a matrix for highly biocompatible materials like hydroxyapatite. It is found that poly lactide can be used as a base for difficult to handle but beneficial and useful additive materials to be present in implants.

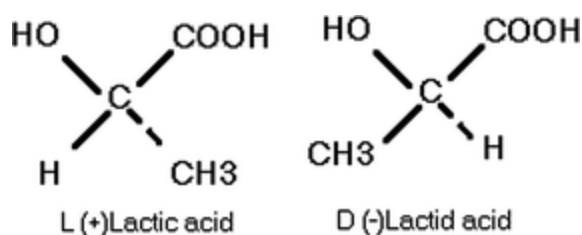


Figure 4 L and D configurations of poly lactide monomers (lactic acid) (Rebelo et al., 2016).

Poly lactide has two configurations, with different polarizations. The two configurations (enantiomers) are named L (levorotatory) and D (dextrorotatory), and the configurations can be seen at Figure 1.4. These configurations can create different properties, such as crystallization speed via adding new crystallization sites in trace amounts of usage (Wen et al., 2010) or blending them with equal proportions to create fully amorphous structures (Mateos-Timenida, 2009)

Poly lactide medical implants are not only a hot research topic, but also an active commercial sector. Figure 1.5. shows the commercially available and used stents on worldwide. Their most prominent and advantageous property of poly lactide stents is to be able to be bioabsorbable (Rebelo et al., 2016). Since lactic acid is an

organic molecule that human body can produce and easily dispose, it has limited side effects compared to the non-bioabsorbable polymers or metals. Ability to be blended with other polymers to tailor its properties or ability to be coated with drugs makes polylactide one of the most ideal materials to be used in medical implantation sector.

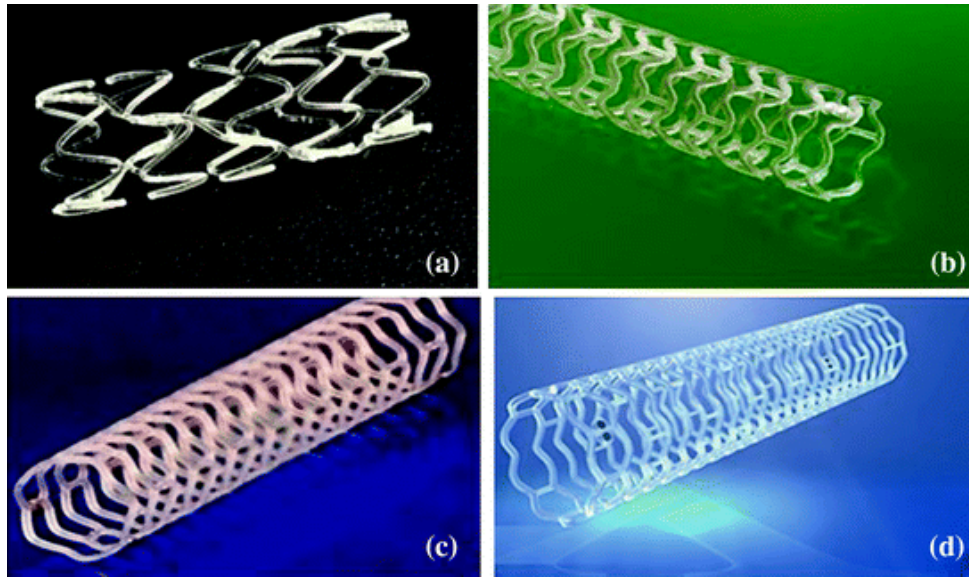


Figure 5 Commercial stents: (a) Igaki-Tamai stent® (b) Absorb stent®, (c) Amaranth stent® (d) Stent DESolve ® (Rebelo et al., 2016).

Poly lactide's biocompatibility and its role on delivering drugs and medical implant production would mean that customization is a crucial aspect. Superior printing characteristics when compared to most other filament materials combined with its high strength and relatively low cost, while not losing biocompatibility status after printing, makes polylactide a well-suited material for FFF technology and on bio-printing.

1.3 Extrinsic and Intrinsic Properties of Additively Manufactured Specimens

Understanding the mechanical properties of 3D-printed parts is necessary for the reliable utilization of 3D-printed components in applications. The parameters that affect the mechanical properties of 3D-printed parts can be divided into two categories, namely, intrinsic, and extrinsic properties. Intrinsic properties are the physical properties of the raw material in bulk form, which directly affect the elastic modulus, mechanical strength, and ductility of the printed part. The thermal processing history and the additives (plasticizers, particles and fibers) can alter these intrinsic properties and impact the strength of the 3D-printed components by affecting the microstructure of the polymer (Rasal et. al. 2010). Extrinsic properties, on the other hand, are unique to the FFF process and include all process parameters such as filament diameter, nozzle temperature, bed temperature, printing speed, raster orientation, and layer thickness. These parameters influence the morphology of the part at the micro and macroscale, and determine the quality of adhesion in between layers, which in turn affect the mechanical properties (Mohamed et.al., 2015).

1.3.1 Extrinsic Properties

There have been a wide range of studies focusing on the extrinsic properties, and these studies show that there exists an optimum for most of the above-mentioned process parameters. For example, increasing layer thickness for a given part reduces the number of heating and cooling cycles, and improves the mechanical properties by reducing the residual stresses in the layers (Sood et.al. 2010). Increasing the nozzle temperature tends to improve the adhesion between the adjacent layers and usually improves the tensile strength of the part (Behzadnasab et. al. 2016). According to (Behzadnasab et. al., 2016) the publish, printing parameters create different results on mechanical properties while printing the polylactide via FFF. 180 to 240 °C nozzle temperatures are tested, and the best

tensile strength is being shown on 240 °C temperature. On the other hand, both the layer thickness and nozzle temperature can only be increased to some extent as they are limited by the dimensional tolerances of the part, and the degradation temperature of the polymer used, respectively.

Raster orientation is another critical parameter; parts tend to be stronger and more ductile when loaded parallel to the raster lines (Odell et. al., 2002). For transverse loading, mechanical properties are inferior due to limited adhesion between the layers. Work shows the comparison of mechanical forces, between different raster orientation and layer thickness values, both by modelling and experimentation, of the samples which are printed by FFF (Yao et al., 2019). Both in modelling and experiments indicate that as the raster orientation approaches to 90 degrees, the tensile property of the printed material increases. 90 degrees of printing of raster means the printing direction of axial loading. The research data indicates that the finer the layer thickness is, higher the tensile properties are.

1.3.2 Intrinsic Properties

When it comes to the effect of intrinsic properties on the mechanical behaviour of 3D-printed parts, the number of studies remain relatively limited, and most studies focus on the effect of various additives. As an example, addition of ~10 wt% polyhydroxyalkanoates (PHA) to PLA provide more than an order of magnitude increase in elongation to failure (Kaygusuz et.al. 2019) and addition of glass fibers to ABS considerably improves the tensile strength (Zhong et. al. 2001). However, the methods to mechanical property alteration without adding any fiber or powder, which produces a composite in return. Works focused on intrinsic properties of 3D printed polymers, without blending additional polymers or strengthening materials is limited.

As adding fibers or powder, or blending another polymer to polylactide, would mean production of a new filament, it would require additional knowledge, material and machinery. Not limited by that, the FFF printer should be tailored for

these new additions. The extruded fibers or powders may clog the nozzle and would need different delivery methods which would mean tailoring FFF printer with new, specialized hardware and integration of software. And blending another polymer to polylactide would mean extruding a new filament, which would require an additional plant for production for the said filament. Both of those methods would be more complex and harder to control and needs a different expertise field. The scope of this work is focused on conventional printing and with commercially available filaments.

1.3.2.1 Crystallization

An important intrinsic parameter that directly affects the mechanical properties of plastic parts is the degree of crystallinity of the polymer. Rapid cooling of a polymer from the melt promotes an amorphous structure and reducing the cooling rate and/or the presence of nucleating agents can induce crystallization. Extent of crystallinity can also be increased by performing annealing treatments above the glass transition temperature, at which the polymer chains gain mobility, and rearrange into a more ordered structure.

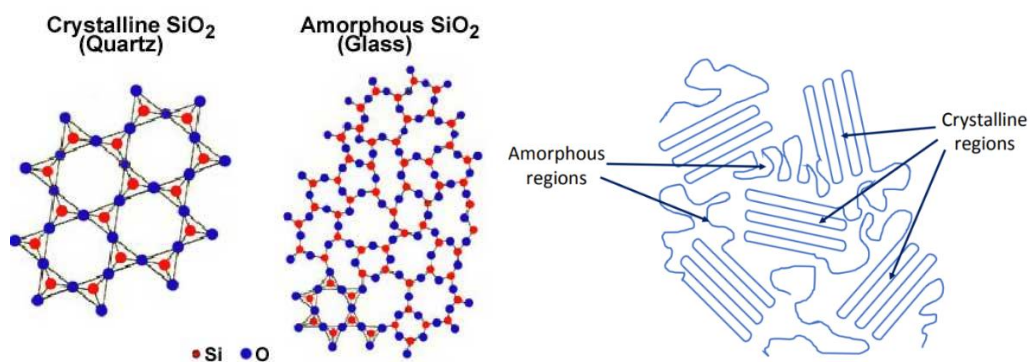


Figure 6 Comparison between SiO₂ (left) and polymer structure (right) (Booth et al., 2017).

The polymers have a chain structure of connected variable amounts of molecules. The complex and long structure of a polymer would mean their microstructural behaviour is different than a ceramic or metal.

As seen from Figure 1.6, the amorphous phase of a polymer is randomly distributed with a tangling formation. If crystallinity is induced, the polymers fold and create a new and ordered structure. Increasing temperatures and slowly cooling down in controlled spaces, and/or inducing new polymers or materials inside the polymer chain can induce crystallinity in an amorphous polymer. Polylactide conforms this polymeric behaviour as the research confirm. According to various literature works (Tabi et al. 2016, Yu et al., 2008), there are various crystalline phases and α' and α phases are the most widely researched and would appear in elevated temperatures with atmospheric pressure conditions and without any force applied. According to the proposed systems, first α' phase occurs, which has a distorted α crystal alignment. Then the crystals would be able to get into a more ordered structure and transform into α crystals (Marubayashi et al., 2008).

As an example, addition of 1 wt% ethylenebishydroxystearamide (EBH) improve the crystallinity of annealed PLA from ~10% to ~40% and the increased crystallinity improves the Young's modulus by 15%, and impact toughness by 100% (Tang et. al., 2012). Annealing amorphous PLA at 80°C increases the degree of crystallinity and can improve elongation at fracture by a factor of three, with a slight increase in the tensile strength of the material (Yu et. al., 2008). Not only the different polymers can be used for introducing new nucleation sites or to hasten the crystal growth rate, but the exact same polymer with different configuration can also be used. The work (Wen et al., 2010) research about the presence and dosage of nucleation agents in extruded polylactide. The work shows that, aside of widely used nucleation agents and its effect on crystallization time, the presence of small amount of D enantiomer of polylactide (%2 as molecular weight) can be used as a nucleation agent in highly dominant polylactide L environment, accelerating the crystallization dynamics. Tsuji et.al. shows at his work that, the mechanical

properties of annealed polylactide specimens are increased. The work concludes that the elevated temperatures of annealing would result in higher crystallinity ratios and results in increase of the tensile strength. In addition to that, elongation at break is lowered by the inclusion of crystalline phases into the material, independent on the crystalline phase and annealing temperature.

Although there is an extensive literature on the effect of crystallinity on the intrinsic mechanical properties of polymers, the implications of crystallinity for FFF remained unexplored. In FFF, the raw material is heated above its melting temperature by the nozzle, and the additive and layered nature of the deposition process results in rapid cooling from the melt. As a result, 3D-printed parts are expected to be predominantly amorphous in nature. While the necessity of the rapid cooling for FFF limits the possibility of tuning the cooling rates for varying degrees of crystallinity, the heat treatment route is a viable option for controlling and inducing crystallization as a post-production process.

Yet as every treatment, inclusion of crystallization via heat treatment would mean some adverse effects that needs to be acknowledged. According to a research (Gupta et al.,1982) the thermal degradation of polylactide can be severe, resulting in a huge drop on molecular weights, at elevated temperatures. Introduction of 70-105 °C medium, on open atmosphere, can result a drop of 6000 mol/gram molecular weight to 3800 mol/gram for 70 °C and 1500 for 105 °C. It is also stated that the melting point of polylactide would drop after degradation under 80 °C, from the found 148 °C to 118-125 °C band, dependant on the time of heat treatment. The research proposes that the degraded specimens have lower melting degrees. Hence, it can be deduced that a protective atmosphere is needed to avoid degradation and oxidation.

Also, literature review (Garlotta, 2001) concludes polylactide and its enantiomers shows that it has a glass transition temperature around 55 °C and melting temperature around 175 °C. The processing temperature of polylactide should not excess of 185-190 °C window. If this temperature bracket is exceeded, unzipping

and degradation of polymer chains can be seen, which would result in loss of molecular weight. As the molecular weight is an important property, ensuring its control is a crucial step.

This would mean that any heat treatment to produce a crystalline polylactide, should take consideration of degradation and oxidation, which would mean loss of molecular weight. According to another work (Rasselet et al., 2010) reduction of molecular weight results in lower mechanical qualities of the treated polylactide material and enhance embrittlement. To remedy this, removal of oxygen from the heat treatment atmosphere is considered.

Another published adverse effect is the density and volumetric changes with the introduction of crystallization on polylactide. The research (Auras et. al., 2004) concludes that the crystallization of polylactide causes on the increased density of the material, which causes on the material to shrink. Another work (Barkhad et al., 2020) shows that crystallinity has an impact on density, as the increased crystallinity ratios increase the density of PLA. In addition to that, according to the same research, pure polylactide can be only crystallized into semi-crystallinity, up to 40 percent crystallinity ratio. The commercial polylactide filaments, which does not list its chemical structure, are expected to 40 percent crystallinity ratio at their maximum. Yet some plasticers and additives are needed for production of filament, or existence of a different configuration of polylactide inside the filament's structure, may increase or decrease the crystallinity ratio.

According to a research (Valerga et al. 2018) the humidity has an adverse effect on polylactide. Hence it is advised to print the specimens with less humidity to show the best potential mechanical properties.

This study aims to investigate the effect of annealing on the mechanical properties of commercially available 3D-printed components. For this purpose, PLA was selected as the material, as it is a well-characterized polymer in bulk form, and it is among the most used filament materials. The obtained filaments did not undergo

any pre-treatment that can change the intrinsic properties of polylactide. 3D-printed PLA specimens were printed in same conditions to ensure same molecular weight, density and crystallinity is achieved and only annealed, afterwards characterized systematically for their structural and mechanical properties. A wide range of characterization techniques combined with mechanical testing provided the structure-property relationships and assessed the feasibility of annealing treatment for improving the properties of 3D-printed PLA parts.

CHAPTER 2

EXPERIMENTAL PROCEDURES

2.1 Specimen Production

An Ultimaker® 2+ FFF printer is used to print dog-bone tensile test specimens. The specimens are manufactured with the guidelines, that are being outlined in ASTM D638 (ASTM Int.). Figure 2.1 shows the specimen geometry. The specimen is first drawn in CAD software beforehand. The used software was Solidworks 2008.

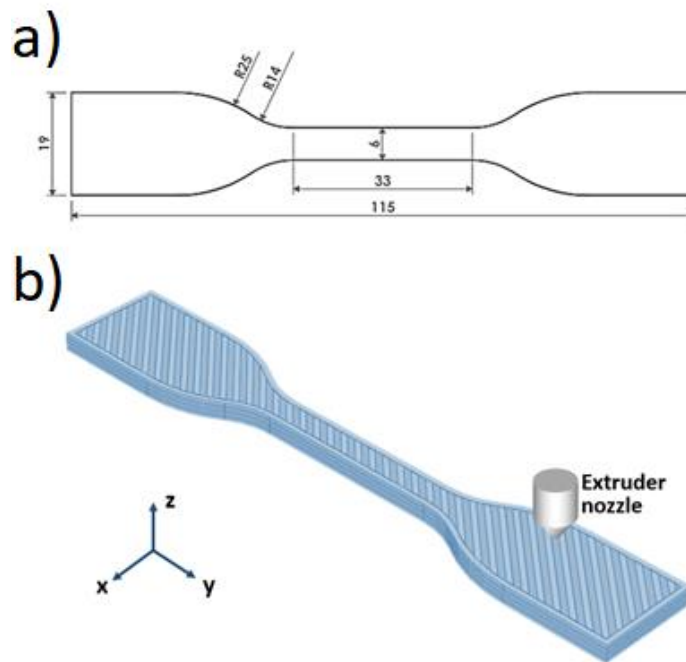


Figure 7 (a) Geometry of the ASTM 638 Type 5 tensile test specimen. Dimensions are in mm. Sample thickness is 3 mm. (b) A schematic showing the printing and raster orientation with respect to the extrusion axis. The given schematic is also valid for the first group specimens.

Table 2.1. Printing parameters.

Nozzle Diameter (mm)	0.4
Filament Diameter (mm)	2.85
Filament Color	White
Layer thickness (mm)	0.2
Printing speed (mm/s)	50
Bed temperature (°C)	60
Nozzle Temperature (°C)	210

To slice the 3D model drawn and define the parameters given above, Ultimaker Cura software is used. Fan power is set zero to avoid warpages during printing procedure. The printer is not enclosed, and the heating plate's temperature only affected the first layer for securing enough adhesion. Printing is done in a place where air flows are limited, so the printing procedure is not affected with fluctuating cooling rates. The nozzle is made of tungsten, which has lower thermal flow than standard brass nozzles, however the printing quality showed satisfactory, and no adverse effect is noted from the usage of tungsten nozzle. The bed is coated with polylactide layer, which is produced by firstly cutting some part of polylactide filament, then dissolved partially in %99,5 purity acetone solution, which is provided by Isolab. Then the solution is poured over the heated bed, with the temperature of 60 °C. The acetone would evaporate and the dissolved polylactide inside the solution would stick to the heated bed. The aim for this procedure is to let the first print layer stick to the same material instead of bed's material, which is made of glass. Filament is annealed beforehand in 60 °C for 24 hours before printing, to eliminate any entrapped humidity, to ensure minimal water vapour was entrapped in the printed specimen.

Two sets of specimens were printed. First group got -45,+45 raster angle with zig-zag configuration. All the specimen for first group were printed with 100 percent infill. No compensation factors or any extrinsic inhomogeneity inducing factors are embedded to the sliced specimens. Three shell layers are printed at the edges for the first set of specimens.

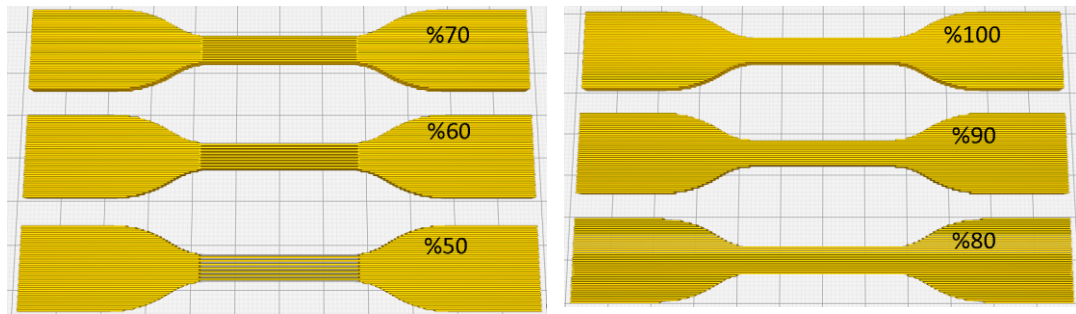


Figure 8 Images of sliced test specimens with different infill ratios.

The second group's printing direction is the horizontal axis, with only pattern of unidirectional line. No shell layers are printed at second group specimens. As it can be seen from Figure 2.2, the infill ratios of the headpiece are remaining the same (%100 infill ratio) yet the neck parts are the only pieces that their infills are changed. The main reason of this is to prevent slippage at lower infill ratios while testing is done. Also, since the headpieces are the parts that are responsible of the load distribution, it is decided that a specimen with a full infill headpiece would be able to distribute the load more homogeneously towards the neck.

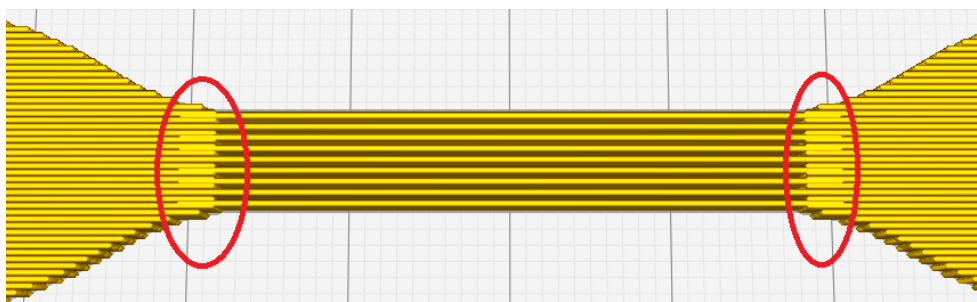


Figure 9 Sliced specimen with %50 infill ratio. The red circles show the welded regions between the headpieces and neck region.

However, the difference of infill at the neck and headpiece would mean there would be weak regions. To alleviate the situation, some portion of the neck piece is embedded into the headpiece. The embedded length into the headpieces is 3.6mm long. This would mean the lower infill part would be welded enough to the headpieces, so the tests would deliver the strength of the neck area, not the strength of the welded regions.

2.2 Annealing

An environmentally controlled EV 018 (Nüve, Turkey) oven annealed the specimens in protected atmosphere. The atmosphere in the oven is first purged with a mechanical pump, down to the point of -0.8 atmosphere. Purging operation is repeated for four times and after reaching -0.8 atmosphere, Linde %99.8 purity nitrogen is pumped into the sealed oven. The specimens were placed in the oven at room temperature and the oven reached the annealing temperature with 4 °C/min heating rate. Upon the completion of the 24-hour annealing at constant temperature, the furnace cooled down to room temperature with 0.85 °C/min cooling rate, and then the specimens were removed from the furnace.

Specimens are annealed as 5 identical specimens for each annealing condition and infill percentages. Full infill specimens with variable temperatures are annealed as a first group, 80-90-100-110-120-130-140 °C. The second group is annealed with 100 °C as a constant annealing temperature, since it is found that 100 C° shows the best mechanical strength data. 24 hours is used for treatment time, but with variable infill ratios, ranging from 50 to 100 percent with 10 percent increments. Half of the printed of the second group were heat treated, while the other half did not to provide a reference and to show the difference of annealing operation for each infill percentage. Two kilograms of weight constrained the specimens during annealing, by placing the specimens under the weight and using a metal sheet to distribute the weight homogenously, with the aim of to prevent any warpage of the specimens. Table 2.2. provides a summary of annealing conditions and sample naming

convention. RS is used for reference sample, while S denotes the sample is annealed with the given temperature after its prefix. I denotes infill ratio and A denotes if the material is annealed or not.

Annealing at atmospheric conditions were also performed by using a hot plate. In this case, degradation of PLA resulted in considerable weight reduction (Gupta et al., 1982). This weight reduction combined with the temperature variations over the specimen during annealing resulted in considerable warpage. As this renders the atmospheric annealing impractical from an application point of view, the properties of such specimens are not investigated.

Table 2.2. A summary of specimens prepared and their naming convention.

Specimen Name	Infill Ratio (%)	Annealing Temperature (°C)
RS	100	-
S80	100	80
S90	100	90
S100	100	100
S110	100	110
S120	100	120
S130	100	130
S140	100	140
I100A	100	100
I90A	90	100
I80A	80	100
I70A	70	100
I60A	60	100
I50A	50	100
I100	100	-
I90	90	-
I80	80	-
I70	70	-
I60	60	-
I50	50	-

After and before annealing procedures, the specimens were weighted, using Mettler-Toledo weight, which have the resolution of 10^{-3} of a gram. It has been found that there is no measurable in the resolution of the weight.

2.3 Mechanical Characterization

In order to understand the impact of annealing procedure on mechanical behaviours, the specimens were tested in tensile conditions. The data of strain to stress values were generated and obtained by using the tensile tests.

A Z250 (Zwick Roell, Germany) universal testing machine with a 10 kN load cell performed uniaxial tensile tests at room temperature at a strain rate of 5 mm/min. An extensometer monitored the elongation of the gauge length. Defected samples that failed prematurely are replaced, re-printed and tested once again.

2.4 Structural Characterization

In order to understand the changes that, both the structure of print and material itself, several characterization techniques are used.

2.4.1 Microstructural Characterization

To analyse the changes that have been underwent on the specimen's structure, a scanning electron microscope (SEM) is used. The SEM is focused on the fracture sites of first group experiment. Zooming is done under consideration of heating effects that SEM focus can create on surface. The zooming is limited by adhering to the fact that SEM can melt the specimen, as the heat dissipated can damage the structure that are meant to be identified. SEM is deployed for first set of specimens.

Microstructure of second specimen were analysed by using optical microscope and the images were captured by the attached camera. Nikon E220 Eclipse optical microscope is used to create images and Toupcam E15 series are used to catch and process the image digitally.

2.4.2 X-Ray Diffraction (XRD)

To identify the phase and structural changes, polymers have two most widely used characterization methods. First is the X-ray diffraction (XRD) if there is crystalline-semi crystalline behaviour is expected. Since the specimens were annealed, crystallinity is expected in the light of literature data. The availability of polylactide XRD reference data in the database of diffraction database, which is used to identify the material afterwards, guided us the work to use XRD as a tool of characterization. Also, XRD is used to determine the purity of the specimens qualitatively. The microstructural characterizations are done for first group of specimens only.

An Ultima IV (Rigaku, Japan) X-ray diffractometer analysed the microstructure of the specimens. We used small pieces cut from the grip regions of the tensile specimens to exclude the possible plastic deformation induced structural changes. The measurements employed the θ - 2θ geometry with a scan speed of $2^\circ/\text{min}$, in the 2θ range 0 - 80° as the most powerful diffractions are at that scanning angle range. Copper is used as a source of X-ray, with its alpha radiation, which is 1.4056 Angstrom at wavelength.

Figure 2.4 depicts the XRD raw graph of PET sample. Machine background is the unusable portion that random scattering of X-rays manage to hit the sensor. Amorphous halo portion is hidden underneath of the crystalline peaks, lifting the peaks upwards. The area between the machine background and amorphous halo line shows the area of amorphous halo. The area situated between the crystalline peaks and amorphous halo is the crystalline peak area. Amorphous samples should be used to understand the range of amorphous halo to fit correctly underneath the peaks.

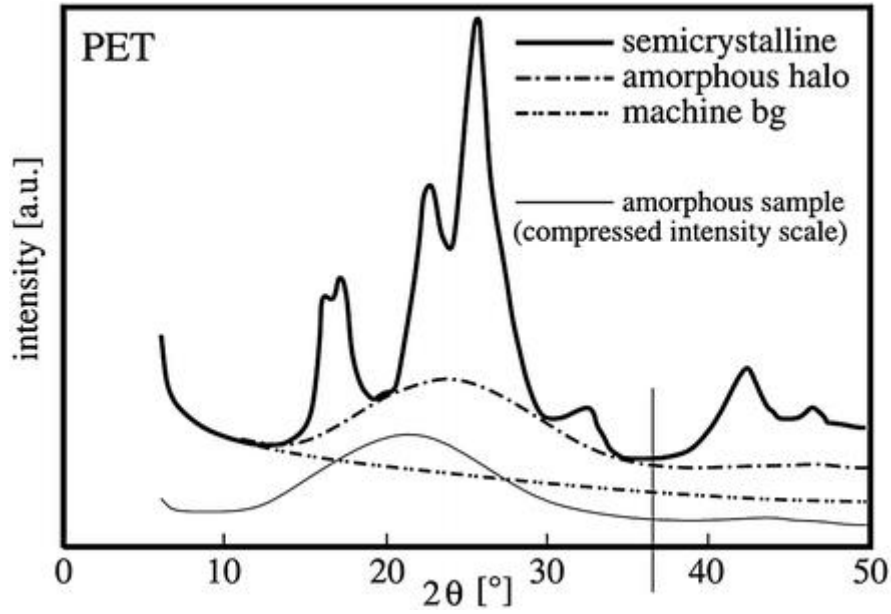


Figure 10 Raw XRD graph of PET sample, showing the machine background (noise), amorphous halo and crystalline peaks (Lamba, 2016).

MDI Jade software is used for refining and processing the raw data. Full width half maximum (FWHM) is used to assess peak coordinates. The noise generated from the X-ray reflections are eliminated, however the amorphous humps are left behind to ensure not to mistake noise to amorphous phase. Peaks are identified by using the database, both from PDF database of METU Central Laboratories and the directories of the software. These peaks are selected and by using Lorentzian approach, the crystalline peak and amorphous halo areas are determined. By using the equation 2.1, the crystallinity percentage is calculated. The calculations are done by the software by fitting the crystalline peaks and amorphous halos over each other and subtracting machine background from the data.

$$X_C = \frac{\text{Area}_{\text{Crystalline Peaks}}}{\text{Area}_{\text{Crystalline Peaks}} + \text{Area}_{\text{Amorphous Halo}}} \quad (1)$$

Crystalline percentage can be calculated via Equation 1, as it shows the calculation of crystallinity ratio (Lamba, 2016). The area of crystalline peaks are divided to the crystalline peak area and amorphous halo area.

2.4.3 Differential Scanning Calorimetry (DSC)

Second characterization method that is used is the differential scanning calorimetry (DSC). A Diamond (Perkin Elmer, USA) DSC analysed the specimens for their thermal characteristics at a heating and cooling rate of $10^{\circ}\text{C}/\text{min}$ in the range $0^{\circ}\text{C} - 180^{\circ}\text{C}$ in nitrogen environment, since polylactide would degrade under oxygen containing environment. The specimen is first melt, then cooled and melt again. The heating curves of post-melting data would not show the crystallization curve of the annealed specimen. Due to that, only the first heating curve is used to understand the crystallinity and other structural changes. Both shifts of melting and crystallization temperatures and the enthalpy and entropy of the melting and crystallization curves are calculated by using the areas under or above the peaks. Figure 2.5 depicts this behaviour in detail.

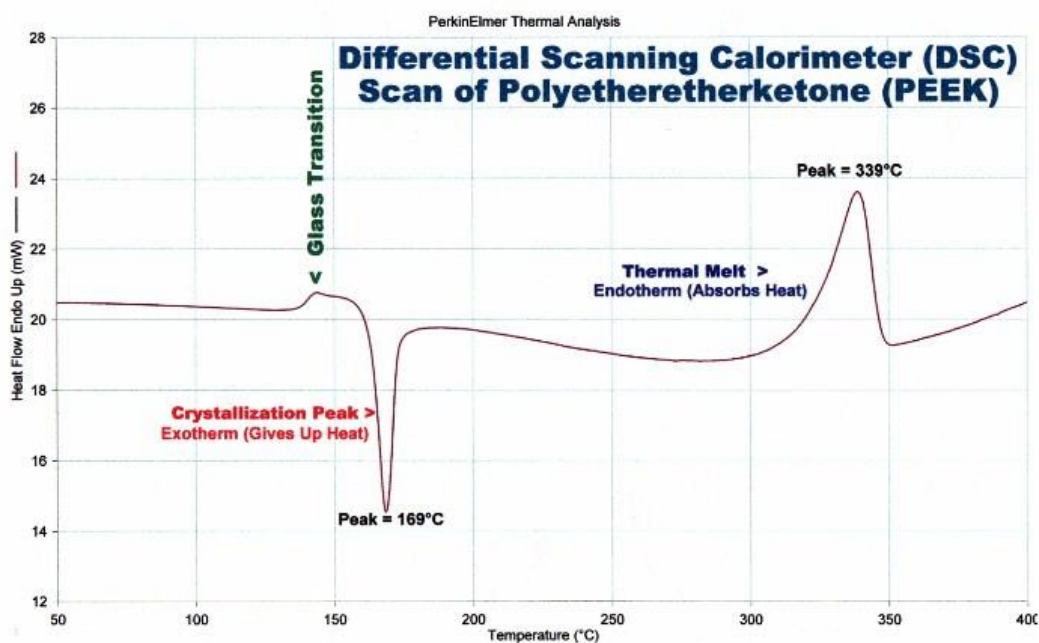


Figure 11 DSC scan of polyetheretherketone. Note that crystallization peak noted is cold crystallization peak (Intertek, 2021).

Figure 2.5 depicts the typical thermal behaviour of semi crystalline polymers.

Afterwards glass transition, the exothermic peak downwards shows the crystallization. Thermal melt occurs as the temperature rises and peak point shows the melting point. The areas between the baseline and peaks are calculated and by using the heating rate, the enthalpies of melting (ΔH_m) and crystallization (ΔH_c) are calculated. ΔH_m^0 is the theoretical fully crystalline enthalpy of the material, which is 93 J/g. Equation 2. is used to determine the crystallinity ratio by using data. (Garlotta, 2001):

$$X_C = \frac{\Delta H_m - \Delta H_C}{\Delta H_C^0} \quad (2)$$

CHAPTER 3

RESULTS AND DISCUSSION

Annealing process is bound to change the behaviour of the material. Yet the range of the change is needed to be discovered and the reasons of the changes would need to be discussed. This section would give the results of both material and mechanical data that are accumulated during the characterization processes. Afterwards, the reasons of such data will be discussed and compared to the other findings with similar research in order to give an understanding.

There would be changes expected in the material afterwards the annealing process along the material's microstructure. In order to discover the changes that annealing process, the analysis procedures of XRD and DSC are used.

3.1 XRD Analysis

XRD is a primary material characterization technique, which is widely used in worldwide. The first step is to ensure the material is primarily polylactide. As the filament is a commercially ready product, it is expected to have trace amounts of impurities and blended polymers.

In order to identify the material's main component and to ensure that the materials produced are mainly polylactide, diffraction data from the database is used. The data obtained from the diffraction database is given at table 3.1.

Table 3.1. Diffraction data obtained from diffraction database, Central Laboratories, METU (Brizzolara et al., 1996).

No.	2Theta	d-Value	Intensity	h	k	l
1	8.87	9.964	1.0	1	0	1
2	12.42	7.124	5.0	1	0	3
3	14.76	5.996	6.0	1	0	4
4	16.69	5.309	100.0	2	0	0
5	19.10	4.642	16.0	0	1	4
6	20.78	4.270	1.0	2	0	4
7	22.38	3.969	6.0	2	1	0
8	24.06	3.696	1.0	2	1	3
9	25.08	3.548	1.0	3	0	0
10	27.45	3.246	2.0	1	1	7
11	29.10	3.066	2.0	1	0	9
12	31.45	2.842	2.0	3	0	6

Since the obtained values from the database, are from isothermally crystallized polylactide in L enantiomer, annealed in 155 °C, the closest annealing temperature (140 °C) is used to compare the data. Hence the data obtained from S140 is used for comparison between 2 Theta, d spacing and area percentage.

Table 4.2. Raw diffraction data of 140 °C specimen. 2 Theta angle values are at leftmost column, and d values are given in angstrom. Peak centers are given at third column and rightmost column is holding the values of percentage area of peaks compared to the major peak.

2-Theta (°)	d(Å)	Centroid (°)	Area%
14.925 (0.018)	5.930 (0.014)	14.856	5.2
16.749 (0.002)	5.288 (0.001)	16.709	100
19.141 (0.007)	4.632 (0.003)	19.093	15.2
22.398 (0.040)	3.966 (0.014)	22.367	2.9
22.519 (0.625)	3.945 (0.216)	23.342	8.1
27.549 (0.010)	3.235 (0.002)	27.509	5.3
29.051 (0.034)	3.071 (0.007)	29.134	3.1
31.176 (0.048)	2.866 (0.008)	31.285	4.7

The identified peaks are given at table 3.2 to list the details of the found peaks. If the data obtained from S140 and diffraction database are compared, it can be seen that several peaks are missing in S140's XRD data. Since the material is semicrystalline, some of these low intensity peaks could not be identified from the amorphous halo. However, the major peaks of (200), (014) and (104) are identified at S140's XRD data with clarity and matches with the diffraction database data, yet with some differences. Minor shifts along the peaks can be noted and the area percentages of S140 are lower than the diffraction database data. Those discrepancies are expected, since S140's material is commercially obtained polylactide with impurities and diffraction database data is obtained by pure polylactide. Second reason is that the annealing temperature difference, as the

diffraction database have data from 155 °C annealing, yet the closest temperature of annealing of our experiment is 140 °C, which is S140 group. 155 C° for annealing is tried yet warpages could not be prevented due to the melting.

Figure 3.1 (a) shows the X-ray diffraction (XRD) results of all specimens. Reference sample (RS) with no annealing shows only an amorphous halo centred around $2\theta = 15.6^\circ$, characteristic of amorphous pure PLA.

Annealed specimens exhibit three major peaks, corresponding to (200), (014) and (104) reflections, and those peaks belong to polylactide as the diffraction database matches the values for the said material. However, there are some other minor peaks that can be seen in the XRD graph. Those peaks are due to the impurities and blended polymers of the filament. Yet the graph does not show any distinctive peak aside of the major peak that is situated near $2\theta = 16.70^\circ$, which is the major peak of polylactide. Only the minor hump located at $2\theta = 36.20^\circ$ does not belong to polylactide. Yet this does not warrant that some other minor peaks or humps are not overshadowed by amorphous halo or major peaks of polylactide.

Figure 3.1 (b) shows a close-up view of the data in the 2θ range of 15-20°. The figure shows that both (200) and (014) peaks first shift towards higher angles with increasing annealing temperatures up to 110°C. At 120°C, there is a rapid shift to smaller angles, and a further increase in annealing temperature shifts the peak to higher angles again.

The findings from XRD shows conformity with the literature findings (Pan et al., 2006). The semi-crystallinity of the specimens would mean that the minor peaks cannot be assessed precisely, aside of the (200) and (014) peaks, and not used to find crystallinity ratios and d-spacing values.

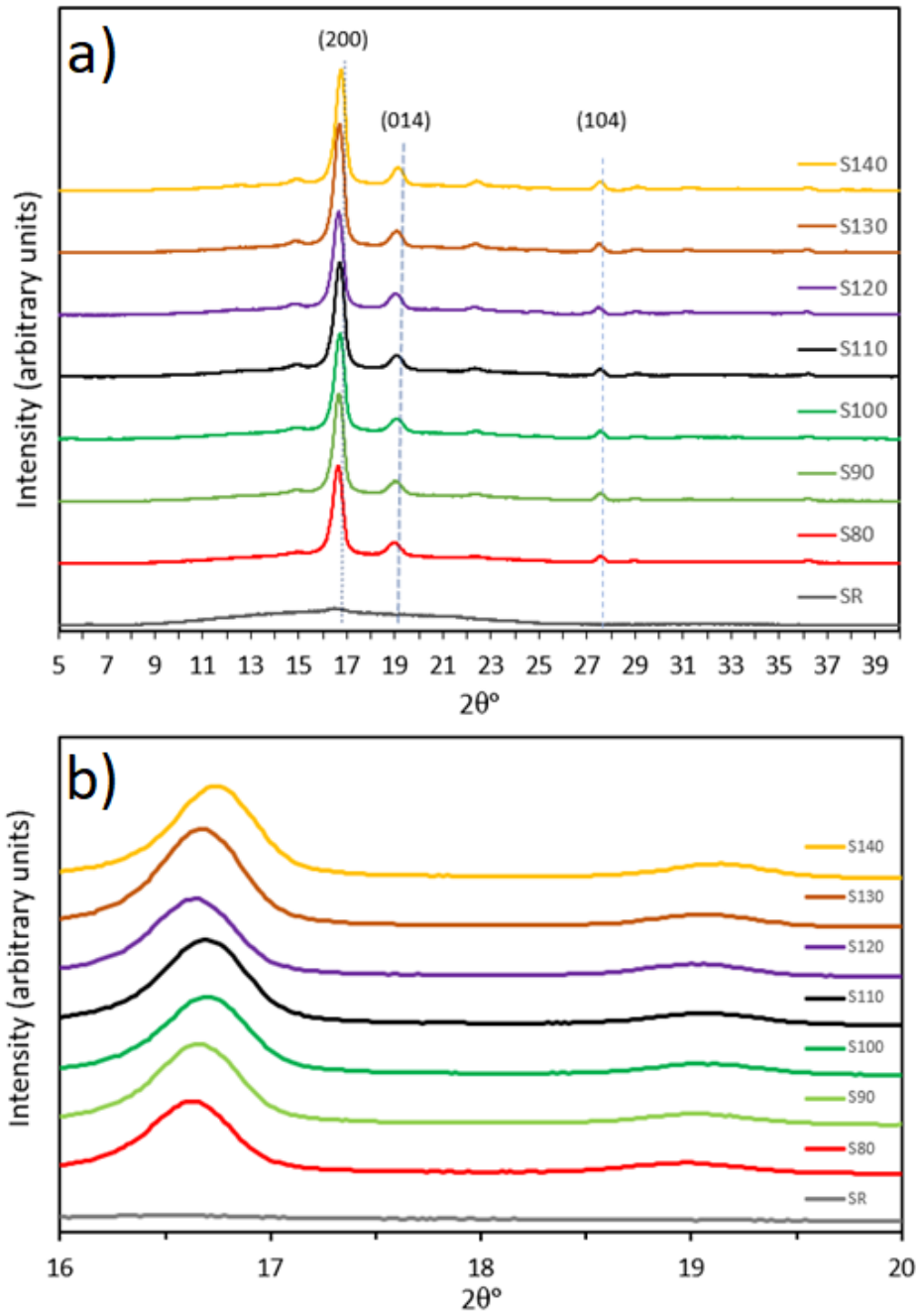


Figure 12 (a) XRD data of as printed and annealed specimens. (b) Close-up view of the (200) and (014) peaks.

In order to determine the machine background and amorphous halo, XRD graph of amorphous specimen is needed. As seen from Figure 3.2, the SR shows amorphous nature and shows two weak peaks.

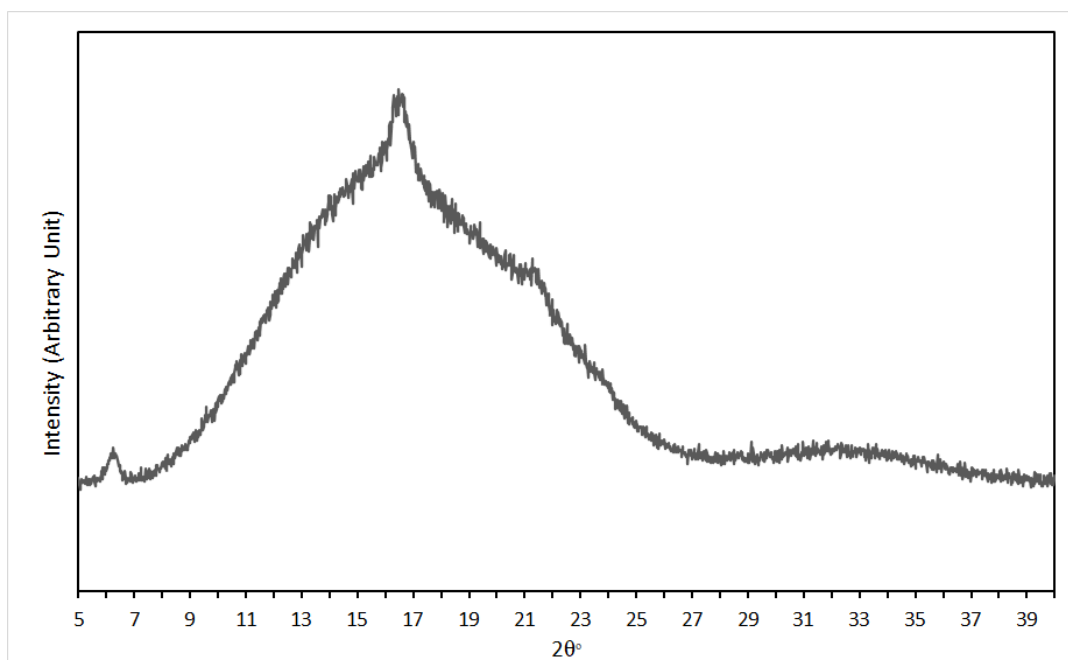


Figure 13 Separate XRD graph driven by raw diffraction data collected from SR sample group. Amorphous diffraction can be easily noticed.

The amorphous peak's centroid angle and the intensity guides the amorphous halo's angular and intensity range. From the graph, it can be deduced that from the angle of 7 to 27, a single amorphous halo is present. Afterwards, there is a secondary minor hump between the angles of 29 to 37.

3.1.1 Crystallite Size Prediction

As the crystalline peaks indicates the nature of crystallization of the material, the shifts of the peaks are valuable data. According to Bragg's law, the peak location indicates the crystallite dimensions. As the peaks shift, it would mean contraction or expansion of the crystallites.

Figure 3.3 shows the d-spacing values calculated by using Bragg's law. The peaks of (200), (014) and (104) peaks are used as the intensities of the remaining peaks were too weak to reliably calculate d-spacing values. The results show that the trends are mostly similar for each peak with small variations. The d-spacing first decreases with annealing, and then there is a jump at the annealing temperatures of 110-120 °C. Further annealing decreased the d-spacing once again, to a minimum value among all specimens at the temperature of 130 °C.

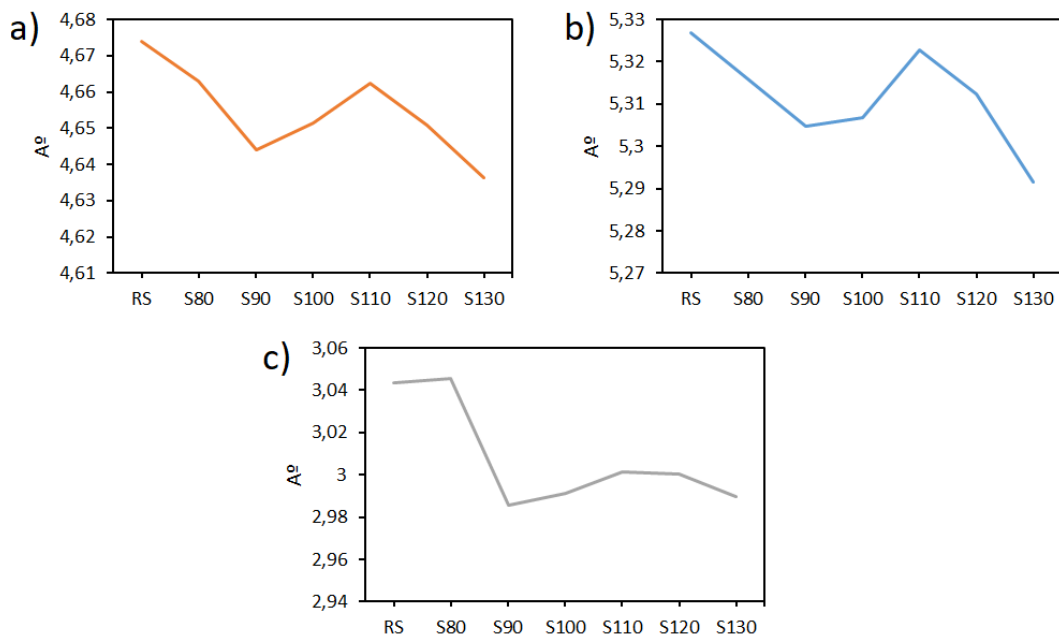


Figure 14 (a) (014), (b) (200) and (c) (104) Miller indices interplanar spacing data for S80 to S140 specimens.

By using the d-spacing data based on each peak we calculated the a, b and c values of the orthorhombic cell through Bragg's law (Bragg, 1913). It is known that polylactide crystals are orthorhombic (Brizzolara et al., 1996).

$$2d\sin\theta = n\lambda \quad (3)$$

The values of d-spacing are found by using the peaks by using the equation 3 which is known as Bragg's law (Bragg, 1913).

$$\frac{1}{d_{hkl}^2} = \frac{h^2}{a^2} + \frac{k^2}{b^2} + \frac{l^2}{c^2} \quad (4)$$

By using the d-values found from equation 3, the a, b and c values can be found afterwards, revealing the unit cell dimensions of the orthorhombic polylactide crystalline cell by using Equation 4.

Equation 3.1 shows the Bragg's law, where d is the spacing between the atoms inside a crystal cell. θ is the angle value derived from the peaks of the XRD graphs. n is the order of the reflection and λ is the wavelength of the incident X-ray beam. As the λ , θ and n values can be found and derived, the interatomic spacing of the given θ value can be found, for each diffraction data.

Equation 3.2 shows the derived Bragg's law, applied for orthorhombic cells. h, k and l values denote the Miller indices of the given plane. a, b and c values are the dimensions of the orthorhombic cell, denoting its x, y and z values of one cell. By using the three values from (200), (014) and (104) planes, the values of a, b and c are found.

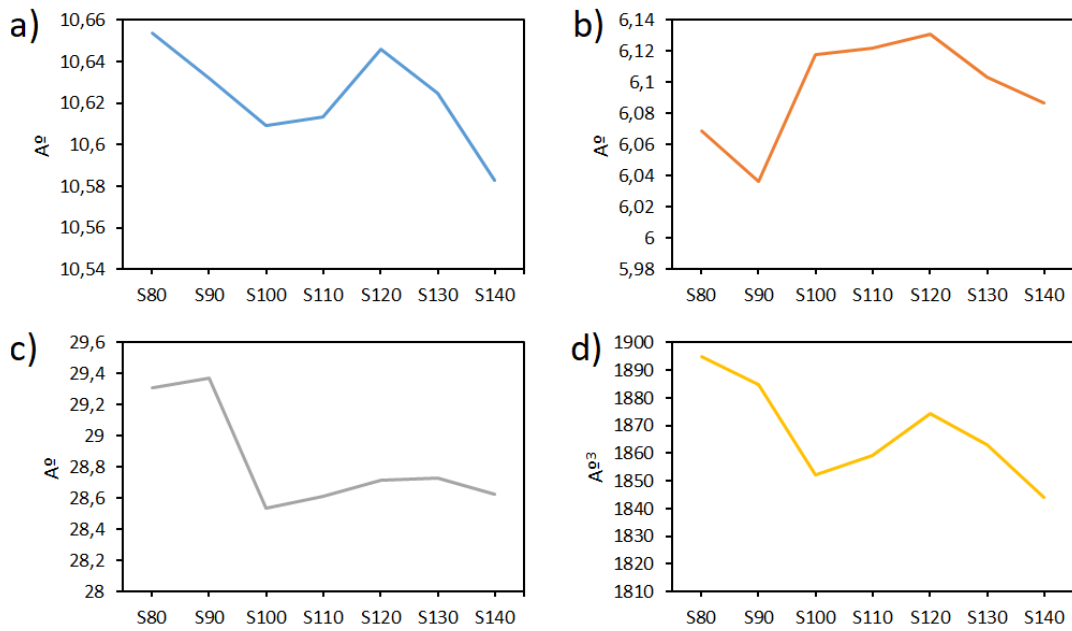


Figure (a), (b) and (c) shows the results from equation 2, versus annealing temperature. There is no complete agreement between the trends, suggesting a complicated process of microstructural changes as it will be discussed.

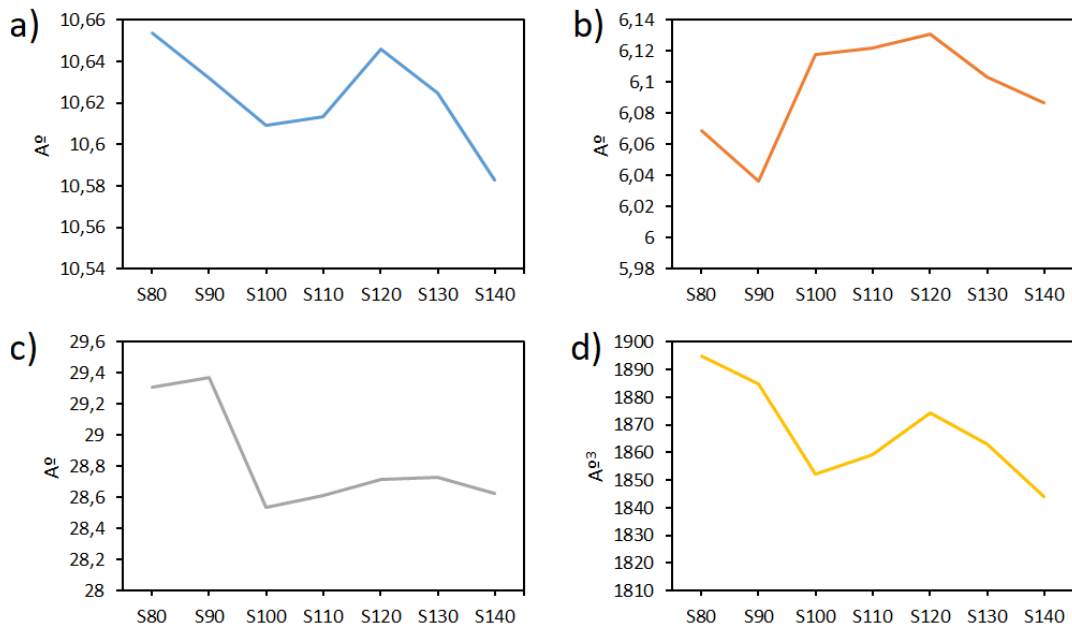


Figure (d) shows the unit cell volume as a function of annealing temperature. As it can be seen, the dimensions of a, b and c are changing, at each different

temperature of annealing. The cell volume first decreases with annealing, until 100 °C. Then there is a regime of expansion up to 120 °C. With higher annealing temperatures, the unit cell starts shrinking and reaches to a minimum value at 140 °C. Same trend can be seen in some of the works (Tabi et al. 2016) at the literature, and the shrinkage at 100 °C then expansion of the crystals after 100 °C is shown.

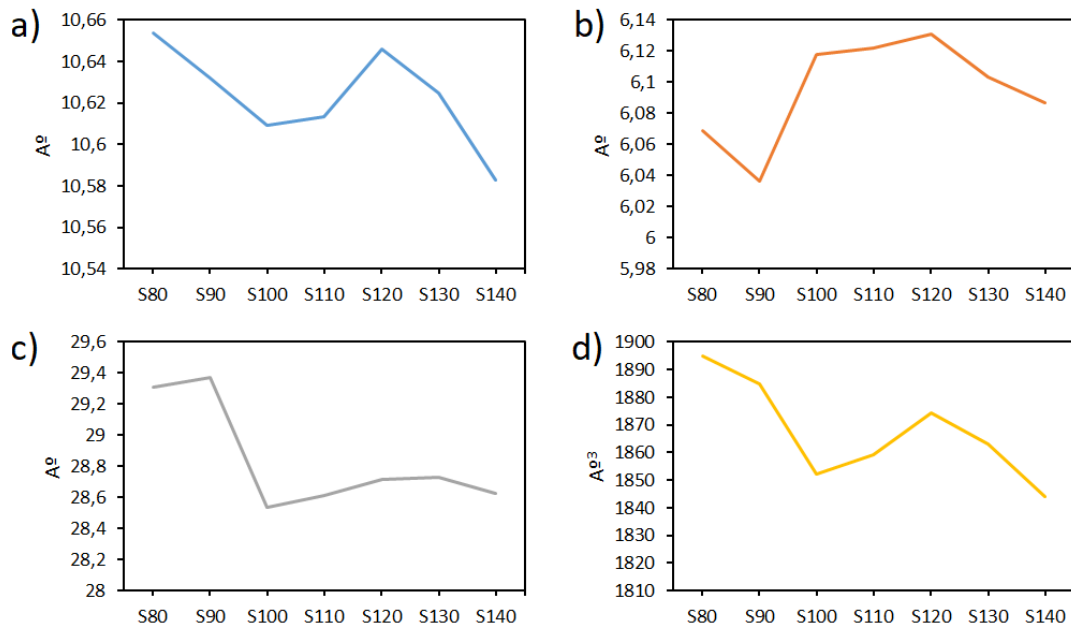


Figure 15 Sample groups and calculated a (a), b (b), c (c) and cell volume (d) values for the orthorhombic cell of PLA crystals.

3.2 DSC Analysis

DSC would be used as the secondary characterization of the polymer. Since it is known from XRD analysis that the material may have trace amounts of impurities and blended polymers in the specimen, the DSC analysis will be done by assuming that the material is purely polylactide, as the other materials cannot be characterized.

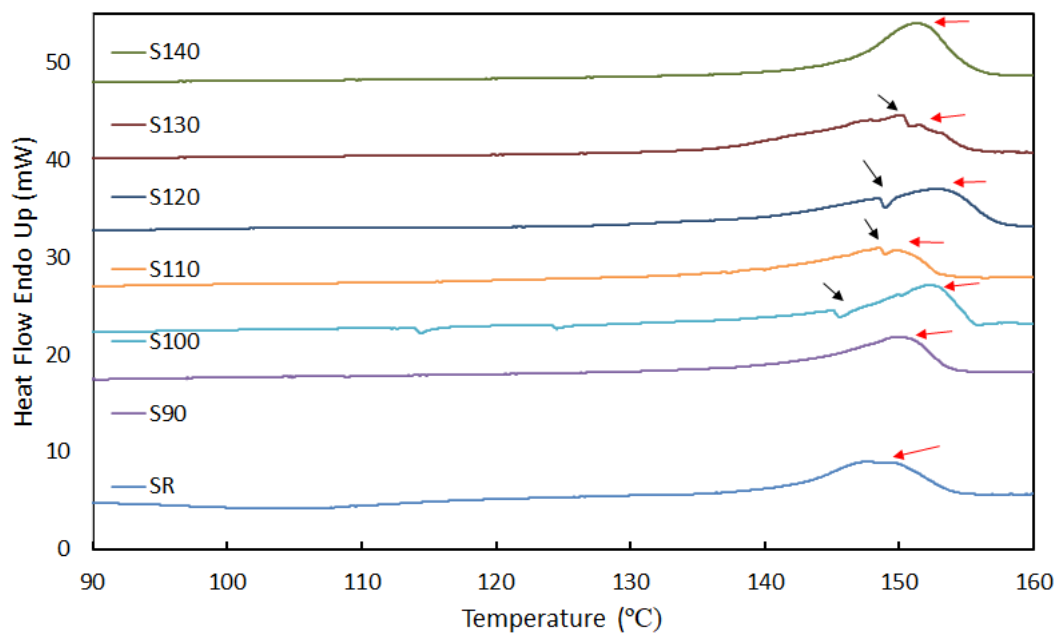


Figure 16 DSC scan under nitrogen purge conditions, with 10 C/min heating/cooling rate. The red arrow shows the melting behaviour and black arrow shows the pre-melting endotherm.

Figure 3.5 shows the DSC data of the specimens with full spectrum of the temperature. Some irregularities and notches can be seen on the figure. The arrows indicate the notches, before the melting occurs. The peaks before the notches are called endotherms and their presence shows the hint of crystalline phase transformation in the specimen. The endotherms are situated right before melting is done. It should be noted that these endotherms start to form at S100-S130 specimen groups. For S140, the endotherm dissolves completely inside the melting curve. Same behaviour can be seen in literature (Pan et al. 2008). At that work, this trend is seen at 120°C annealing process and continues until 140 °C annealing temperature, with 360 minutes of annealing duration. Even if the annealing durations are not matching, the curves and the endotherm before melting matches the same profile. Zoomed DSC graph near melting points can be seen from Figure 3.6.

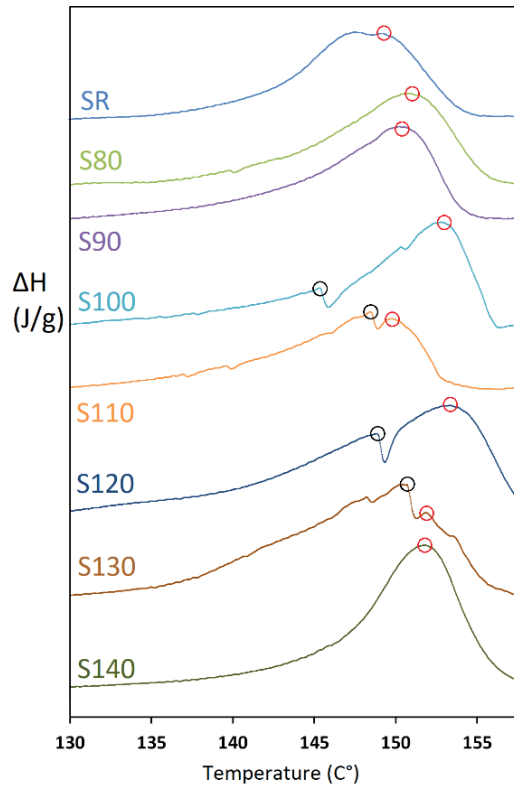


Figure 17 DSC scan for the specimens, zoomed in near their melting temperature to indicate the melting points and endotherm peaks. Melting points are shown with red circle and endotherm peaks are shown with black circle. Endo flow is upwards and the curves are fit above each other for easier comparison. Y axis does not show the absolute values.

The irregularities are mainly due to the endotherm curve that is located before melting peak. The endotherm peaks are shown with the black circle and melting peaks are shown with the red circle. As the heat treatment temperature increases, the endotherm temperature also increases and shifts towards melting further. Note that at S140, no endotherm is observed, signifying the endotherm, and melting peaks are fused. It should be noted that the same phenomenon can be seen at some studies (Tabi et al., 2016). From the work, it has been shown that from 80 to 100 $^{\circ}\text{C}$ anneal, a single melting is shown and concluded that only α' phase is presented in

the material. After 100 °C, it has been shown that a new endotherm is presented, α' and α phases coexist until 140 °C. At 140 °C, it has been shown that only α remains as the crystal phase. The same can be said for the specimens tested, aside of 100 °C. In the works of literature (Tabi et al., 2010 , Pan et. al, 2008) pure polylactide shows a single endotherm at 100 °C and it has been concluded that a single crystal phase of α' is present at that temperature. In current work, there is an endotherm located at 100 °C, implying coexistence of α' and α . This shows that the used polylactide filament is not pure polylactide, yet at the same time, the impurities cannot be detected via XRD and the DSC results give similar results. The comparison of DSC graphs between literature and current work can be seen at Figure 3.6 and Figure 3.7.

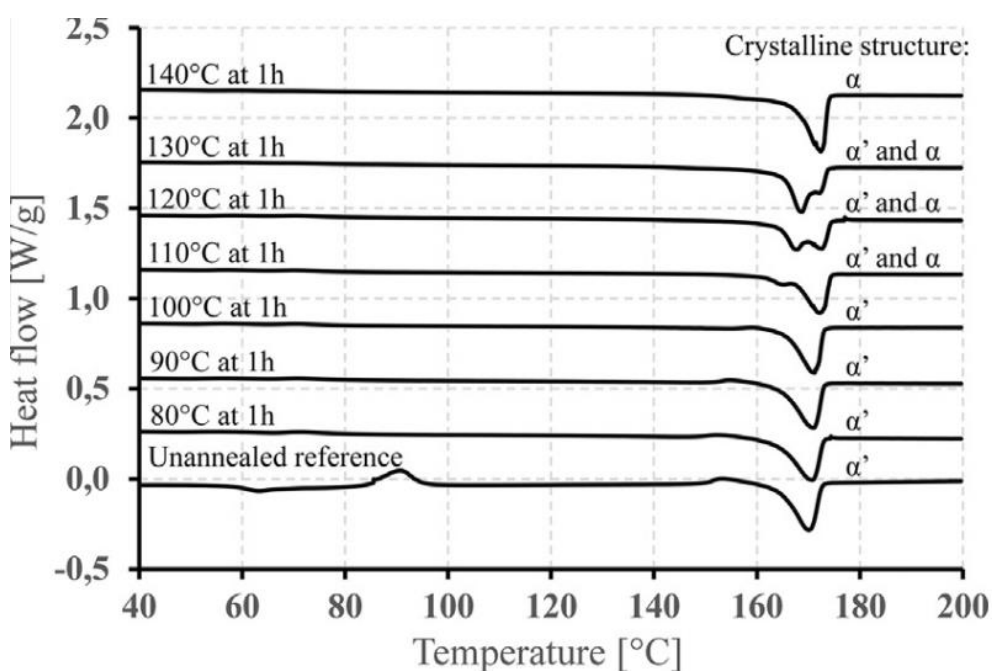


Figure 18 DSC scan from literature data. Annealing temperatures and hours can be denoted at left and crystalline structures at right of the thermal graph. Endo flow is downwards. (Tabi et al., 2016)

Table 5.3. Melting enthalpy (ΔH_m), cold crystallization enthalpy (ΔH_c) and melting point (T_m) comparison between specimens

Specimen Type	ΔH_m (J/g)	ΔH_c (J/g)	T_m (°C)
RS	22.98	-14.46	147.57
S80	22.65	-	150.38
S90	25.58	-	149.93
S100	23.41	-	152.40
S110	24.49	-	148.54
S120	31.10	-	152.90
S130	33.80	-	151.81
S140	34.78	-	151.37

Table 3.3 shows the distinction between values of the specimen. Enthalpy of melting first decreases at S80. Yet cold crystallization enthalpy is eliminated, indicating the material did not undergo further crystallization during the thermal test and solely ΔH_m value would be useful for attaining the crystallinity for the heat-treated samples. S90 shows a gradual increase at enthalpy of melting and at S100, the ΔH_m decreases once again. At S110, the incremental increase can be spotted, yet after that, S120, S130 and S140 specimens show considerably larger values of ΔH_m if they are compared to other specimens.

DSC curves and data is used to understand the composition of PLA, in terms of d-enantiomer or l-enantiomer formation. Studies show (Srithep et al., 2019) that fully l-enantiomer (PLLA) has a melting point of 152 C°, melting enthalpy of 25.7 J/g, cold crystallization point of 116.9 C° and cold crystallization enthalpy of 23.1 J/g. D-enantiomer of PLA (PDLA) is found with the data of, melting point of 175 C°, melting enthalpy of 56.7 J/g, cold crystallization point of 92.2 C° and cold

crystallization enthalpy of 16.5 J/g. If this data is compared with the data obtained from the second melting properties of polylactic samples from DSC, which would be melting point of 149 C°, melting enthalpy of 22.3 J/g, cold crystallization point of 117.4 C° and cold crystallization enthalpy of 21.0 J/g. It has been shown that increased D phase on PLA leads to an incremental reduction on cold crystallization point. Since the specimen shows the cold crystallization point of a fully PLLA sample, and the values of melting enthalpy, melting point and cold crystallization enthalpy are conforming the literature PLLA values, it can be said the specimen's polylactide is fully composed of L-entanthiomer.

3.3 Comparison of XRD and DSC Results

Figure 3.7 shows the crystallinity ratio calculated from XRD and DSC scans. The crystallinity ratio, that are found both by DSC and XRD scans show an increasing trend. However, DSC and XRD does not agree in results as trend, for S140 specimen group. There are differences between the values of XRD and DSC scans, however this difference is expected, as both analyses have different methodologies of characterization. DSC scan is volumetric and applied all over the volume of the material, yet the XRD analysis can only be done for a limited penetration and only skin of the material can be scanned effectively.

The research shows that there is a difference between core and skin of the crystallinity, up to four percent, even after an annealing procedure. Same research shows that the difference between DSC and XRD crystallinity analysis, as the difference is up to ten percent (MasPOCH et al., 2004).

Another research (Doumeng et al., 2021) shows that a semicrystalline polymer, PEEK, shows different crystalline values, when density, XRD, DSC and Raman are used to determine the crystallinity values. XRD values showed an underestimation and DSC values showed an overestimation when the values are compared to the different methods. It has been shown that, the average of both values can be used to determine a more correct estimation of crystallinity, especially after %25

crystallization. The reason behind this over and underestimations, is due to the nature of tests. It is discussed that, as DSC would mean heating up the polymer, which would melt the polymer, yet it would also create a heat treatment itself over it, crystallizing extra sites that were not done. The same literature work discussed that XRD values are underestimated because of the amorphous halo and some parts of the crystalline peaks are absorbed under the said halo, formed due to the amorphous phases. For defence of our work, DSC analysis is done by using the literature data (Tabi et al. 2016, Pan et al. 2007) and 10 C°/min is used as a heating rate for DSC, to ensure no extra crystallinity is added into the material when DSC analysis is done. Yet there is no efficient method to counteract the underestimate of XRD is found.

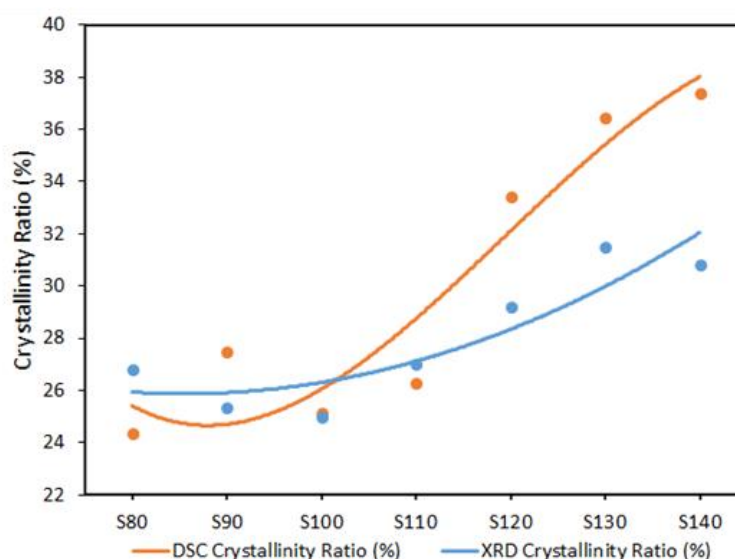


Figure 19 XRD and DSC crystallinity ratio comparison. The crystallinity data is fit to a curve, with a third-degree polynomial. Note the distinctive jump at 120 C°.

The same effect of skin and core, for 3D printed specimens are not yet discussed. The reason of this difference can be due to the fact that the both of the characterisation methods are not absolute and have different advantages and disadvantages. Heating during DSC may have increased the crystallinity ratio calculated, as DSC analysis can only be done by melting the specimen. Another

case can be for XRD, as the research (MasPOCH et al., 2004) shows the difference of crystallinity ratio between skin and core of the material, as this work did only take XRD data from the surface of the material. Even if both analysis shows some difference, they show that the material is semi crystalline and have similar trends and values.

3.4 Effect of Annealing on Crystallinity Level

Formation of one phase to another phase is a complex phenomenon, be it amorphous to a crystalline phase or a crystalline phase to another crystalline phase. As the temperature increases, the energy of the polymer chains increases. Higher energy would also mean that the mobility of the polymer chains would be increased, as the material closes towards its melting temperature, the chains would motion in the material in a more fluid manner.

According to the thermodynamic laws, at every different temperature, the equilibrium of different phases is dependent on the energy of the molecules. The energy of the material is expressed in temperature and pressure. As the material phase is solid and the transformation is undergone between different crystalline phases and the amorphous phase, only the temperature can be used as the energy ingredient, as the pressure in the solid materials is set constant. Gibbs free energy is a well-known and established equation that shows the reasoning behind phase transformations.

$$\Delta G = \Delta H - T\Delta S \quad (5)$$

In equation 4, Gibbs free energy equation is presented. ΔG denotes Gibbs free energy, ΔH is the enthalpy of the proposed system, T is the temperature in Kelvin of system and ΔS is the change of entropy of the system.

ΔG is an indicator for the given system's stability in terms of phases. If the calculated ΔG number is less than zero, it would mean that the system is favored on change towards the proposed phase change. Zero would mean the system is at the

equilibrium and higher than zero denotes the system is against the proposed phase change. Equation 4 shows that different T values would mean different ΔG values as enthalpy and entropy values are not expected to change in a constant pressure system.

It is known from the literature survey and the experiments; PLA have at least two crystalline phases that is formed in the heat treatment range, α' and α crystal phases, and a single amorphous phase. All those phases are in an equilibrium with different gradients at different temperatures. This can be found by utilizing ΔG values for each crystalline and amorphous phase. Having at least two different phases inside the specimens would require different enthalpy and entropy values recorded or calculated.

Start of crystallization or transformation of one phase to another, can be done by, first, nucleation of new crystal sites. Those crystal sites then expand and form crystals. The speed of growth those crystals and nucleation site densities, is set by some models depending on the thermodynamical models like Gibbs free energy. One of the models is called Lauritzen-Hoffman, which is a combination and derivative of the thermodynamic laws. This model, however, exceeds the scope of this work as it would require numerous different analyses. Literature (Foglia et al., 2020) shows the Lauritzen-Hoffman plots for polylactide. It has been shown that the theoretical start of α' phase transformation is 90 °C, growth rate peaks at 110 °C and stops at 135 °C. For α phase, transformation starts at 105 °C, growth rate peaks at 120 °C.

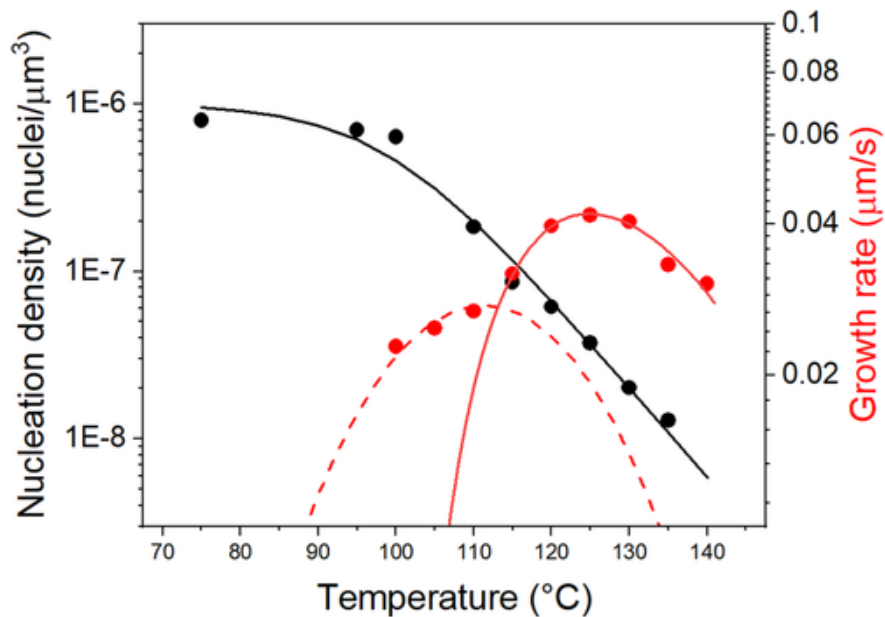


Figure 20 Lauritzen-Hoffman plot for nucleation density and growth rate. Red dots and lines show the growth rate and black dots, and lines show the nucleation density. The scattered red lines represent α' phase and full red lines represents α phase plot. Note the increased crystal growth rate as temperature rises. (Foglia et al. 2020).

The work (Pan et al., 2008) shows that the increased temperature of heat treatment for PLA also increases the percentage crystallinity. Also (Tabi et al., 2016) proposes that α' phase turns to α phase, at 100 °C, proposing a crystalline phase change from one to another, implicating the presence of at least two crystalline phases. (Zhou et al., 2009) suggests, the crystallization directions change from two dimensional expansions, changes into a three-dimensional expansion as the temperatures rises. (Foglia et al., 2020) work proposes that 100 °C is the critical temperature for α' to α phase transformation, and both phases can coexist together and the transformation would start to favor on α phase after 120 °C. It is also proposed that DSC scans would show a lower melting temperature for α' phases and endotherms before melting for α' and α phase mixtures, and single melting point for α only phase. (Marubayashi et al, 2008) shows the XRD peak shift of annealed polylactide for 80, 110 and 140 °C temperatures. It is shown that the 80

°C has α' phase, 110 °C has the mixture of α' and α phases, and 140 °C annealed specimen has α phase only.

The experimentations that are done to discover the effects of annealing should be subdivided to understand the implications on the results of crystallinity ratio, cell volume and DSC endotherms.

Crystallinity ratio graph of Figure 3.8 shows the trend of the crystallinity ratio for both XRD and DSC values. It can be seen that, pre S110 specimens, have a significant lower crystalline value. However with the S120, higher annealing temperatures result in a considerable jump of crystallinity ratios, which can be discovered by both DSC and XRD analysis, and which they both agree on. The temperature of 120 °C can be thought as the point where thermodynamic equilibrium of crystal formation of α phase is considerably more favored than the α' . As (Zhou et al., 2009) proposes the three dimensional growth of α crystals, which the work also showed higher growth rate and in result, higher crystallinity percentage as a result. A conforming result is also present in other work (Pan et al., 2008), showing higher crystallinity for higher annealing temperatures.

Cell volume is another thing that can show the crystallite phase transformation. Figure 3.4 shows the cell volume of the crystallites. Research about polylactide crystallization (Marubayashi et al., 2008) shows the values of orthorhombic dimensional change between α and α' phases. It is shown that α phases are more compact, especially in terms of a and b values, while values of c component of orthorhombic cells are found constant. As seen from Figure 3.4 (c), the c value does not change greatly after 90 °C annealing operation, yet values of a and b changes as the heat treatment temperature changes. The cell volume lowers down up to the point of 100 °C of annealing temperature. Then a gradual increase can be seen then after 120 °C, the cell volume shrinks once again. This could be seen as the packing of the crystallite size and increase of density of the crystalline phases whenever the cell volume decreases, and expansion of the crystallite unit cell as the cell volume increases. These changes are showing that different crystal formations

underwent at the temperatures of 100 °C and 120 °C, which are the inflection points of the cell volume values. This peculiar behaviour between 100 °C and 120 °C is noted by other works (Pan et al., 2007, Tabi et al., 2016), as crystallization times, crystallite sizes and growth rates show discrepancies. Yet the understanding behind this behaviour is beyond the scope of current work and would require more analysis.

Lastly, DSC endotherms are shown at Figure 3.6., right before melting occurs. It is shown on other works (Marubayashi et al., 2008 , Tabi et al., 2010) that similar endotherms are occurred with similar heat treatment operations. However, another work proposes that the occurrence of endotherms can be a result of incomplete crystallization. Some studies show that, the crystallization time for polylactide differs with different temperatures (Tsuji et al., 2006). The study suggests the crystallization of the PLA films is completed, under the spectrum of 90 C° to 140 C°, in a timespan of less than 50 minutes. Another study, shows that the crystallization speed fluctuates, starting with 16 minutes, dropping down until 100 C° (3.47 minutes for half crystallization time), and 110 C° is the second fastest (3.51 minutes for half crystallization time) for PLA films, then rising up to 22 minutes, for 125 C° treatment. These data both concludes that the time given for the crystallization of the specimens, is enough for reaching the maximum crystallization percentage and the reason of the endotherms before melting is due to the mixture of crystalline phases of α and α' , not because of incomplete crystallization, but because of the system is at equilibrium with the said phase mixture.

3.5 Mechanical Properties

The mechanical properties of both temperature controlled (SR-S140) groups and infill controlled (I50-I100) and infill controlled annealed (I50A-I100A) groups are mechanically tested to understand the effect of annealing, with both different temperatures and infills ratios.

3.5.1 Mechanical Properties of Temperature Controlled Specimens

Figure 3.10 (a) and (b) shows the average ultimate tensile stress, average strain at breakage and average resilience unit, for the specimen groups. It can be easily seen that, for first three treatments of, S80, S90 and S100, result in a better average ultimate tensile stress value. As the temperatures of the heat treatment increases, after S100, the stress values start to drop. After S120, it can be seen that the ultimate stress values got lower than the untreated sample group. Strain values also show a similar trend, with some differences. S80 shows the best result, for strain data, then shows a staggering formation, as S90 strain data drops, and S100 rises again. The average strain values, of the remaining heat-treated groups show less average strain at breakage, lowering its values cumulatively. From the resilience data S90 and S100 are the only specimen groups, which has the improved resilience, compared to the untreated SR specimen group.

Figure 3.10. (c) shows the elastic modulus values and trends over the annealing operation. The values show a gradual increase as the annealing temperature rises. This behavior is expected as it is known that the increased crystallinity amongst the polymers and polylactide, increases the elastic modulus of the material (Tabi et. al. 2016). The reason of this behavior can be seen in the microstructure of the crystalline and amorphous polymers. Highly ordered and stacked chains of polymers would be denser than the amorphous, randomly scattered polymer chains.

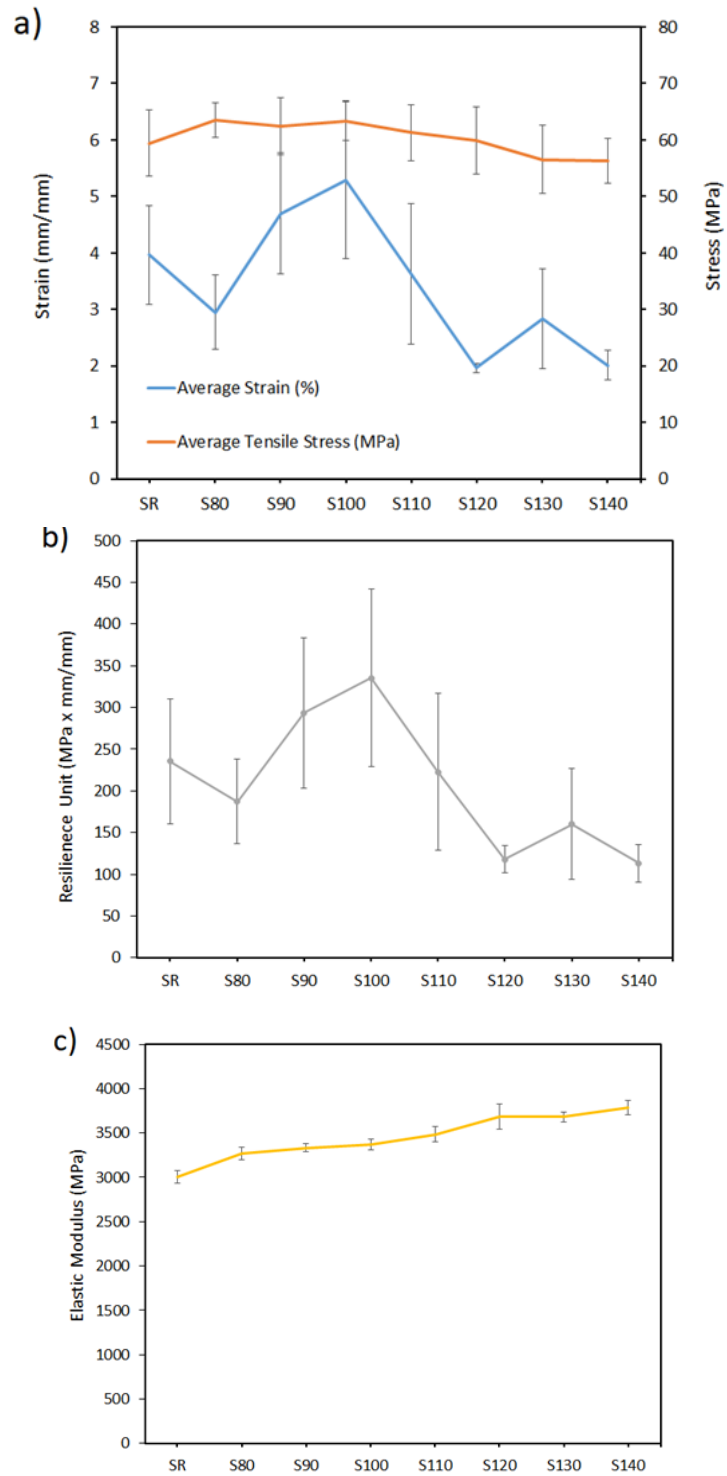


Figure 21 Ultimate tensile stress and strain (a), resilience unit (b), and tensile modulus (c) results. The values are average values of the tested specimens.

The tensile tests also confirm the enantiomer of polylactide in the specimens. Literature work (Srithep et al., 2019) concludes that PLLA shows a better tensile strength, strain and elastic modulus value if it is compared to PLLA to PDLA blends, or fully PDLA material. Fully PLLA specimen shows 50 MPa tensile strength, %5.5 strain and 1200 MPa elastic modulus, while PDLA shows 23 MPa tensile strength, %2.5 strain and 1080 MPa elastic modulus. Stress data shows more than 50 MPa for stress data and the strain data for the unannealed specimen is %4 at average. These data shows that the specimen printed is showing properties, identical to the PLLA. Hence, it can be said the material would be mainly constituted with PLLA molecules, not PDLA. Any blend of PLLA/PDLA also shows a lower value of stress than pure PLLA, so there is no implications on literature data that the strengthening effect of d-enantiomer.

The behavior of ultimate tensile stresses, can be attributed to the, both of the increased crystallization and denser microstructure, and the residual stresses produced due to the shrinkage and thermal cycles. Recent works (Li et al., 2020) about porosity and the consecutive heating and cooling operations showed that, the thermal cycle occurring during the printing procedure, can attribute to cracks, deformation, or reduction of integrity of the printed surface. Since the annealing procedure is done by slow cooling rates (0.85 °C/min), and the time given is much longer than the literature crystallization values (51 minutes, given by Tsuji et al. 2006) would mean there is enough time for crystallization and cooling without any major residual stress. The effect of any thermal cycling from annealing procedure should be very low, compared to the printing procedure, as the print is cooled in open air condition.

Addition to the deformations and cracks that are formed due to the thermal cycles due to the printing, the introduction of shrinkage, due to the smaller crystallite sizes and higher density due to the first amorphous to α' crystal, and then from α' to α phase transformation. This trend can be seen both from the Figure 3.4. (d), as it shows the shrinkage of crystal unit cells, but also on external data (Auras et al.

2004).

Hence it can be discussed that the thermal cycles due to the printing and the shrinkages along the specimens lower the mechanical properties of the printed, then annealed specimens. Yet the introduction of crystal phases into the material, results in higher mechanical results on injection moulded specimens (Tabi et al., 2016). It can be said that those two mechanisms compete each other; as the temperature increases, crystallinity is increased, hence the mechanical properties improved. However, the increase of temperature would promote, shrinkage until 100 °C, and limited expansion until 120 °C, and shrinkage until 140 °C once again. Those could mean cracks and deformation along the heat-treated specimens. Moreover, the possibility of thermal hysteresis can be discussed, as the shrinkage-expansion-shrinkage can result in weakening along the print.

Figure 3.11. shows the graph, with different annealing temperatures showing different tensile strength (Tabi et al. 2016). As it can be seen that each of the treated specimens has better tensile strength and modulus than the un-treated, reference data. It should be noted that the production type used in this literature experiment is mould injection. Hence there is no micro features that, neither thermal cycle of printing or the shrinkage of crystallites have the same impact on the specimens.

If the data from both Figures of 3.11 and 3.10 are compared, it is clear that the graphs does not show conformity. Figure 3.10. shows a rapid deterioration after 100 °C treatment temperature, while Figure 3.11. shows stagnant trend of tensile strength values, yet always higher than the reference sample. As the thermal cycle on printing is constant for each specimen, the reason of rapid deterioration of mechanical properties for higher temperature ranges cannot be from printing only. However the printing procedure would mean voids and gaps would present inside the specimen and the residual stresses and cracks that may have formed after shrinkage-expansion-shrinkage cycles, which would have much more effect on a porous structure than a fully filled specimen, amplifying the effect of the shrinkage cycles.

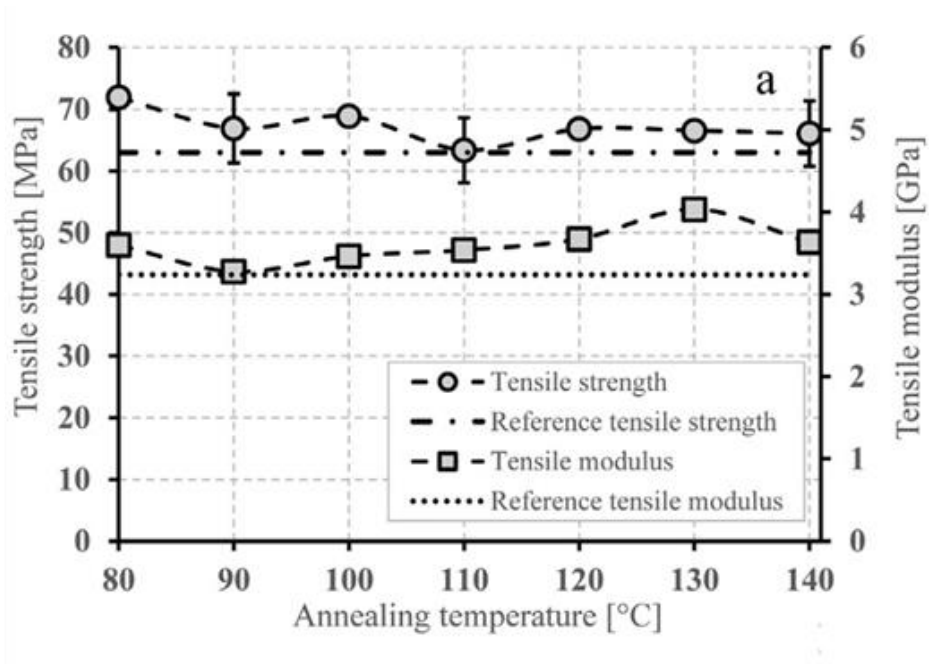


Figure 22 Annealing temperature versus tensile strength and modulus (Tabi et al., 2016).

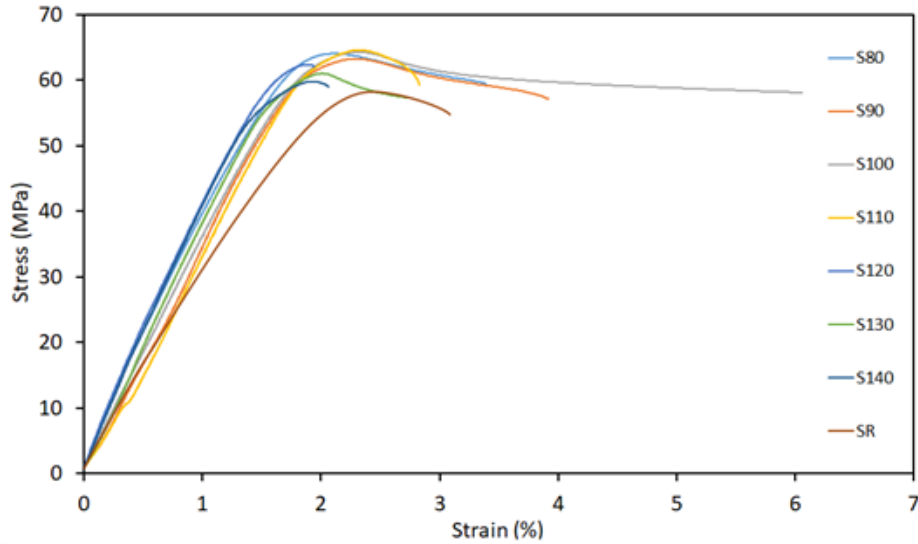


Figure 23 The stress-strain graphs of all specimen groups. Note that the given result is for one specimen in each group.

Figure 3.12 shows the tensile test results, for each specimen group. It can be seen

that for each group, the formation of the stress-strain curve is similar; performing fracture near 60 MPa point, and an elastic deformation area followed by a plastic deformation area, and then fracture. The plastic deformation area differs from one group to another, however there is no discrepancy between the groups.

3.5.2 Mechanical Properties of Infill Controlled Specimens

Figure 3.13 shows the force versus infill ratio of the specimens. The highest infill would give the best result in terms of total force, and it would suddenly drop at 90 percent infill. The resisted force would gradually be increased as infill decreases, up to 70 percent. Second dramatic drop can be seen at 50 percent infill.

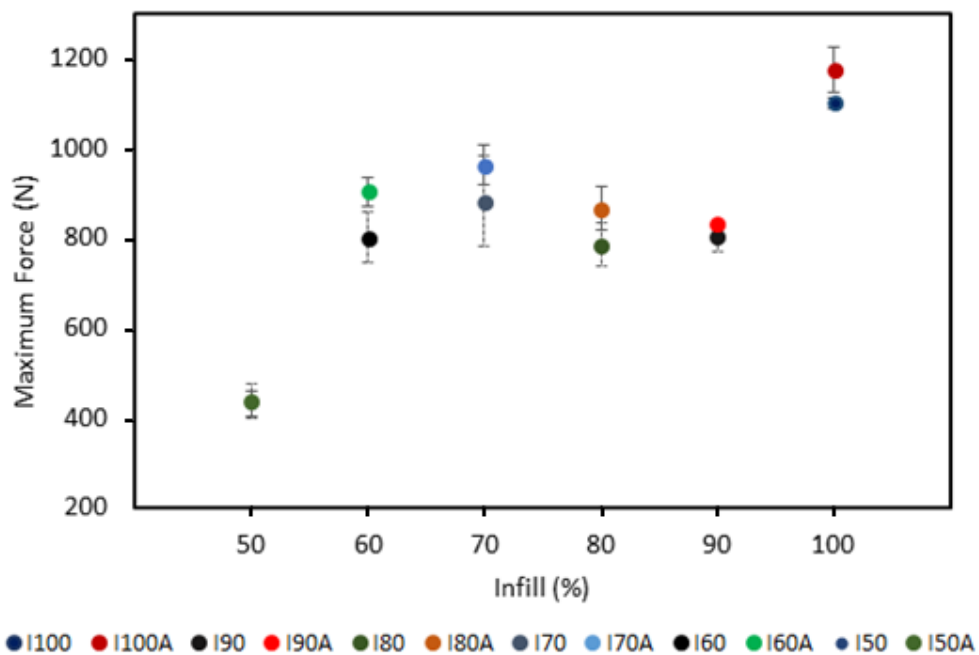


Figure 24 Force versus infill ratio graph. Deviations in the test groups can be seen by the bars. Variations between heat treated and untreated specimens are shown. Suffix of A denotes annealing and I denotes infill percentage.

The effects of treatment can be easily seen too. Figure 3.13. shows the variations

between heat treated and non-treated specimens. The effect of treatment is always positive in terms of force. However, the range of effect is different for each group. The most beneficial treatment is on 60 percent infill specimen. Least benefited specimen by the heat treatment is the 50 percent infill.

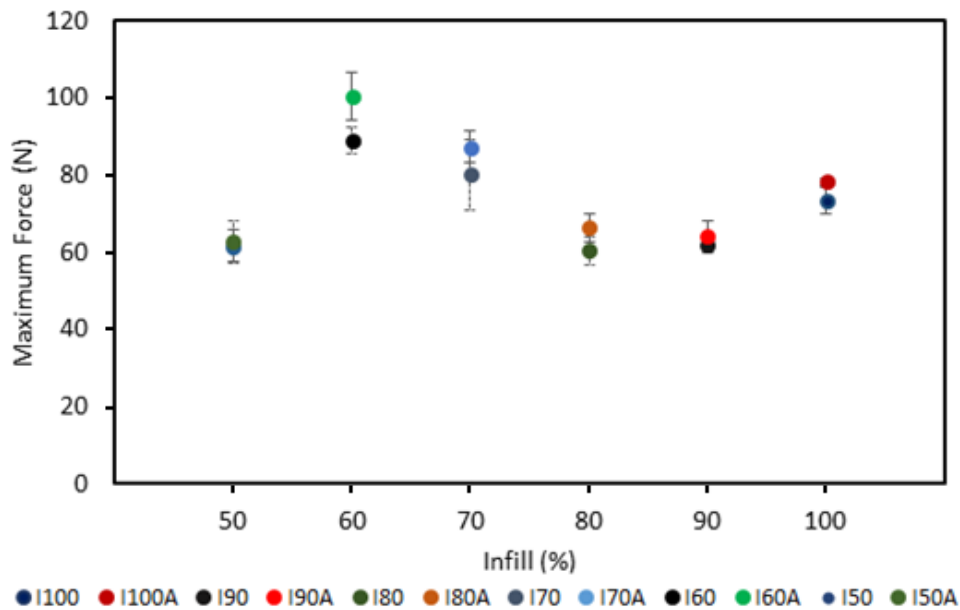


Figure 25 Force per layer versus infill graph. Deviations in the test groups can be seen by the bars. Variations between heat treated and untreated specimens are shown. Suffix of A denotes annealing and I denotes infill percentage.

Figure 3.14 shows the force per layer data. As the different infills would result in different numbers of layers that are printed on the neck region of the material, it would mean the total force would not be enough to understand the effectiveness of the infill. The force per layer trend would be showing the efficiency of layers per infill, in terms of tensile resistance. 60 percent infill with heat treatment would have the most efficient force per layer ratio. Heat treatment gives positive effects on the tensile resistance per layer and for every specimen. Also, the 60 percent infill shows the most benefited specimen group from the heat treatment. And the least effective one is the fifty percent specimen group.

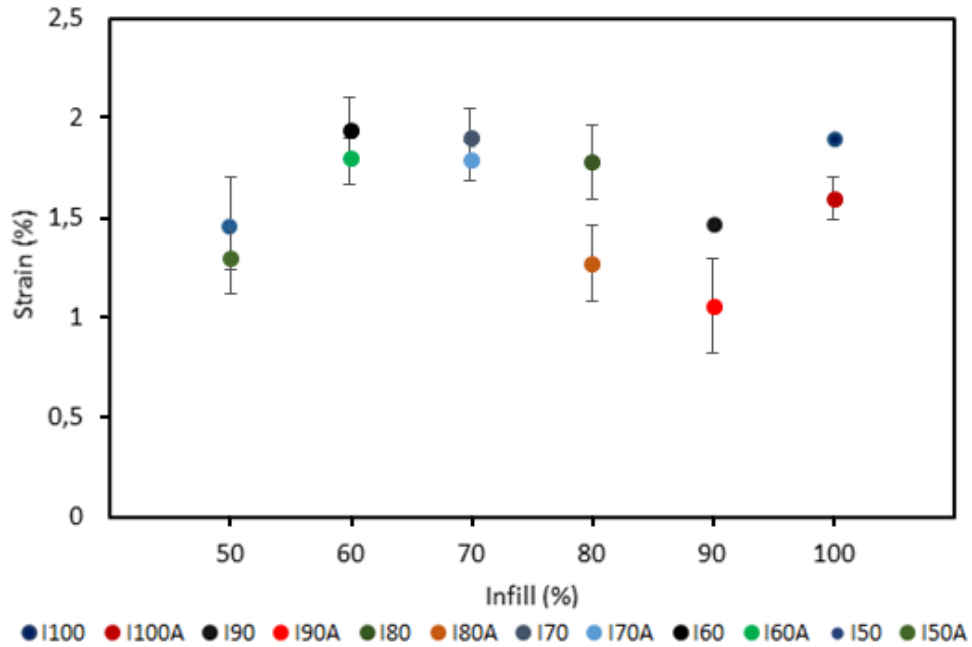


Figure 26 Strain versus infill graph. Suffix of A denotes annealing and I denotes infill percentage.

Figure 3.15 shows the strain versus infill ratio. Highest strain can be seen at sixty percent infill ratio without heat treatment. The least strain can be seen at the ninety percent ratio infill with heat treatment. The heat treatment is affecting negatively on strain values. Most affected specimen group is 80 percent infill, and the least affected group is 70 percent infill specimens, from the heat treatment operation.

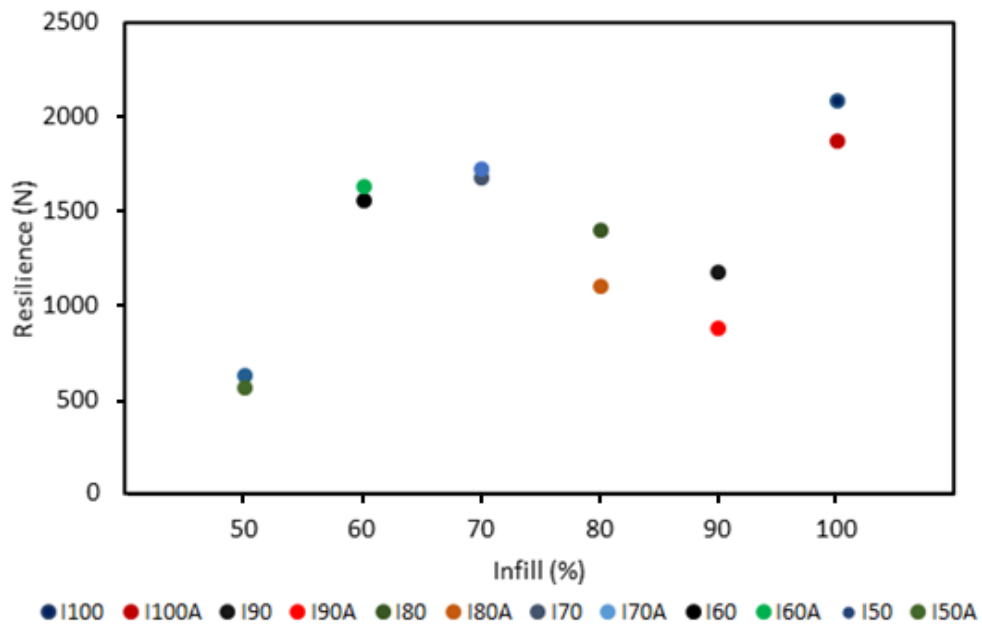


Figure 27 Resilience versus infill graph. Suffix of A denotes annealing and I denotes infill percentage.

Figure 3.16 shows the resilience versus infill ratio. Best resilience values are at hundred percent infill ratio, with no heat treatment applied. Least resilience can be seen at fifty percent infill with heat treatment applied. The trend shows a mixed result about the heat treatment operation. At 60 and 70 infill percent specimens, resilience is affected positively by heat treatment yet other specimens show the exact opposite. Reason of this behaviour can be discussed, within the light of micrographs. The 80-90-100 percent infill prints have more constraints as the printed layers are connected to each other, with X, Y and Z directions. However, 50-60-70 percent infill print layers are connected with Y and Z directions. This can be discussed as a reason of the reduced strain ratios, hence reducing resilience. The reduction of strain values of annealed specimens can be traced in Figure 3.15.

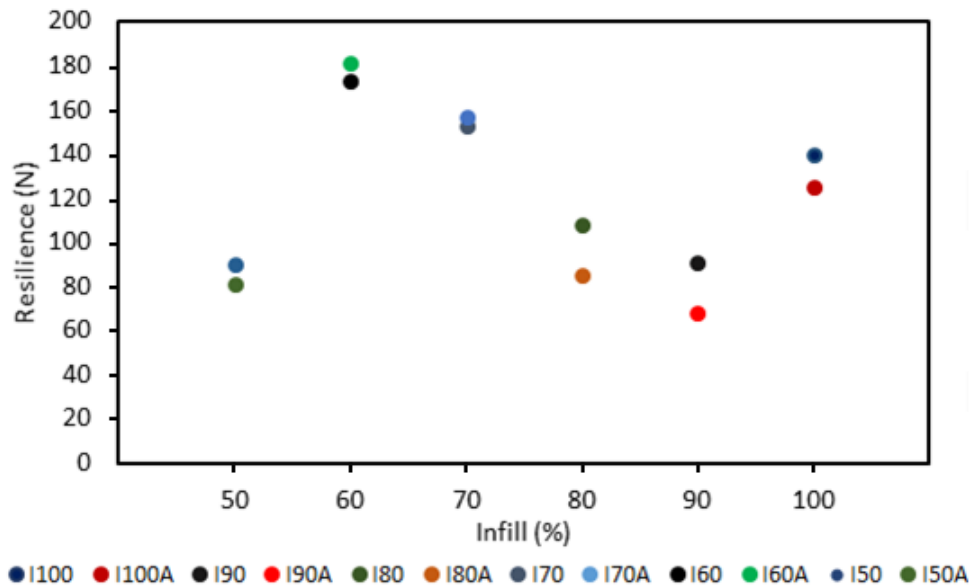


Figure 28 Resilience per layer versus infill graph. Suffix of A denotes annealing and I denotes infill percentage.

Figure 3.17 shows the resilience per layer versus infill ratio. 60 percent infill with heat treatment shows the best result, as it shows the most efficient specimen for mechanical resilience. Trends are mixed for the heat treatment, as the heat treatment on 50, 80, 90 and 100 infill percent specimens show lower mechanical resilience as 60 and 70 infill percent specimens show beneficial results from heat treatment. Reason of this behaviour is the same with the one which affects the total resilience which is discussed above. The 80-90-100 percent infill prints have more constraints as the printed layers are connected to each other, with X, Y and Z directions. However, 50-60-70 percent infill print layers are connected with Y and Z directions. This can be discussed as a reason of the reduced strain ratios, hence reducing resilience. The reduction of strain values of annealed specimens can be traced in Figure 3.15.

3.6 Micrographic Examinations

Micrographic examinations for both temperature and infill-controlled specimens are shown in this chapter. Both SEM and optical microscopy is used to understand the micrographs of the specimens.

3.6.1 Micrographic Examinations of Temperature Controlled Specimens

Figures 3.18, 3.19, 3.20 show, the SEM pictures taken from the fractured part from the SR, S80 and S120 specimen groups. The SEM pictures of SR group, shows the fusion of the printed shell part, with several defects and gaps on it. The raster part does not show any visible defect, or unfused part, as the sandwiched visual of printed layers are expected. Both the raster and the shell part, shows the signs of brittle fracture, as the fractured parts are fractured with a cleavage facets, showing blocky, straight and smooth surfaces especially on the shell surfaces.

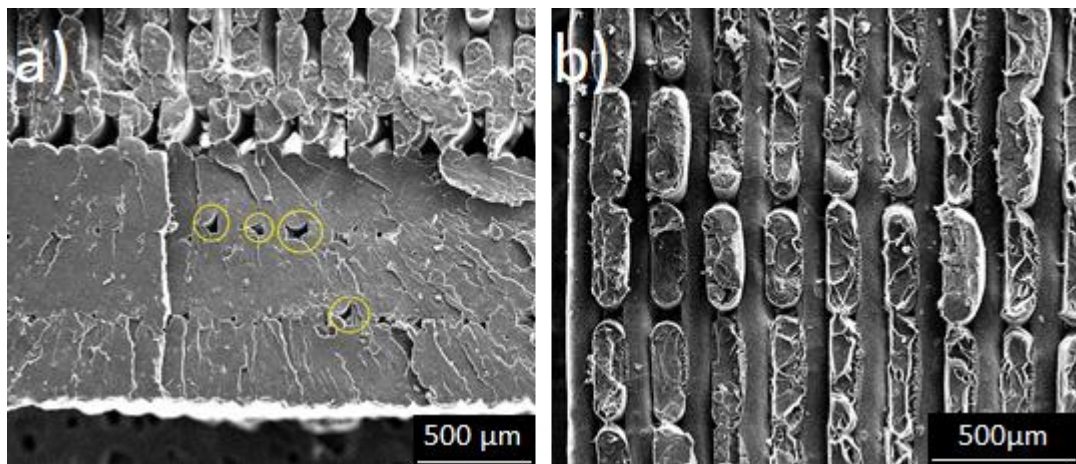


Figure 29 SEM pictures of SR specimens. Left picture shows the shell part, and right picture shows the raster part. Note the defects of the shell part, and the gaps shown by yellow circles.

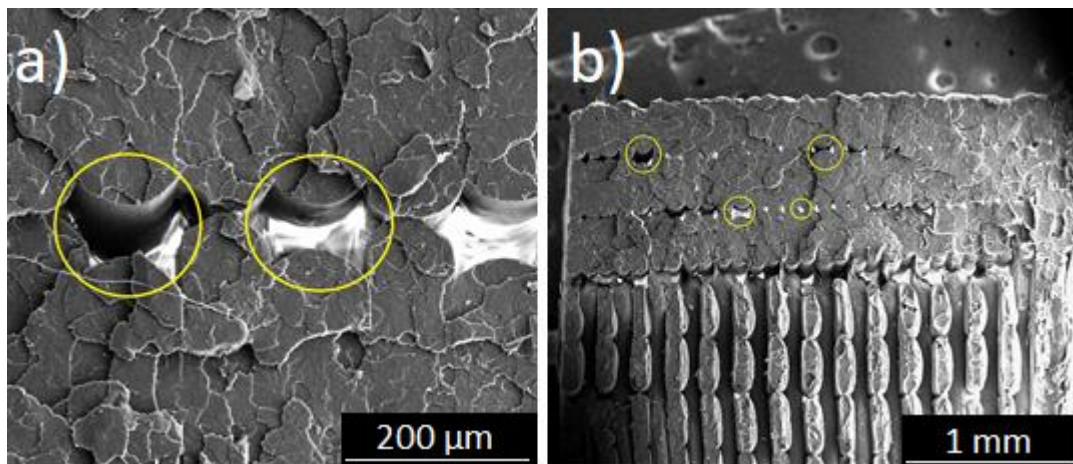


Figure 30 SEM pictures of S80 specimens. Left picture shows the shell part and its defects, and right picture shows the raster and shell part combined. Note the defects of the shell part, and the gaps shown by yellow circles.

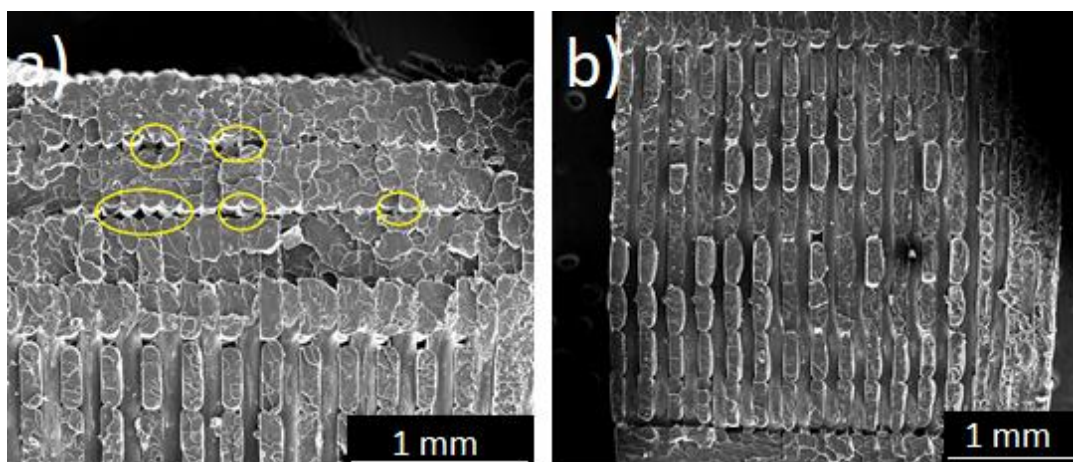


Figure 31 SEM pictures of S120 specimens. Left picture shows the shell part and its defects, and right picture shows the raster part. Note the defects and the gaps shown by yellow circles.

S80 specimen's SEM pictures, reveal the sites of defects are larger and more in quantity. The printed layers of the shell can be easily seen, as the gaps are continuous and ordered. These gaps also discern shell thicknesses and height. These gaps can be a result of the shrinkage of crystallite cell volume. As the cell volume of crystallites lowers, the printed layers, could shrink, and the gaps

between the layers, could get bigger. This can be easily seen, by the SEM pictures, in Figure 3.19. The raster part shows similar morphology, compared to SR raster part.

S120 specimens shows more pronounced gaps and defects. Also, the beads of each printed shell layer can be easily discernible, from the Figure 3.20. The increased density of polylactide and the increased pack density of crystalline phases, can be the reason of this behaviour. The SEM pictures, of the fractured surfaces of S120, shows the brittle fracture morphology, as the same cleavage facets can be spotted over the printed layers, with the different levels of fractured surfaces, instead of micro void coalescence of a ductile fracture.

3.6.2 Micrographic Examinations of Infill Controlled Specimens

The micrographs got from different infill ratios are given below, showing its details with different magnification, and at its fracture sites.

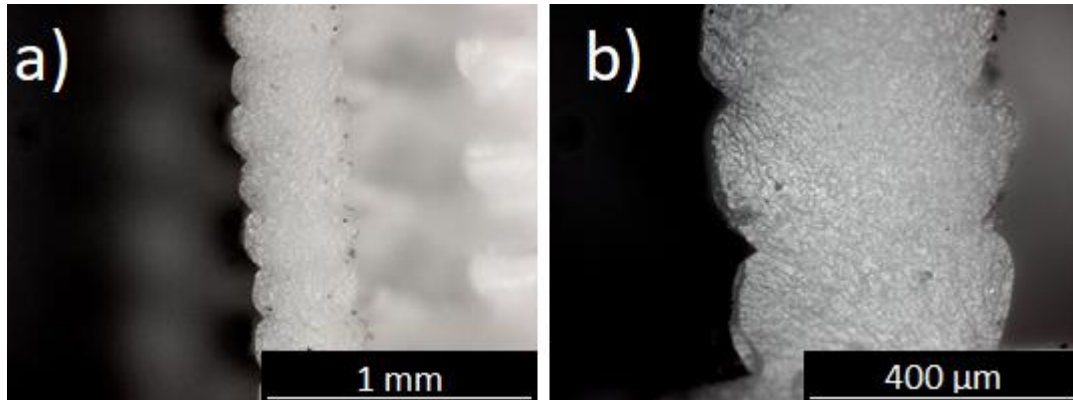


Figure 32 Micrographs of 50 percent infill printed specimen. Left micrograph shows 40x and right micrograph shows 100x magnification. The micrograph is taken from the fracture site.

The fracture shows the brittle nature of PLA. There is no crevice or propagated cracks spotted at the micrographs. The layers are stacked homogeneously, and printing is done as it is expected. There are no artifacts between the layers and

shows no sign of delamination.

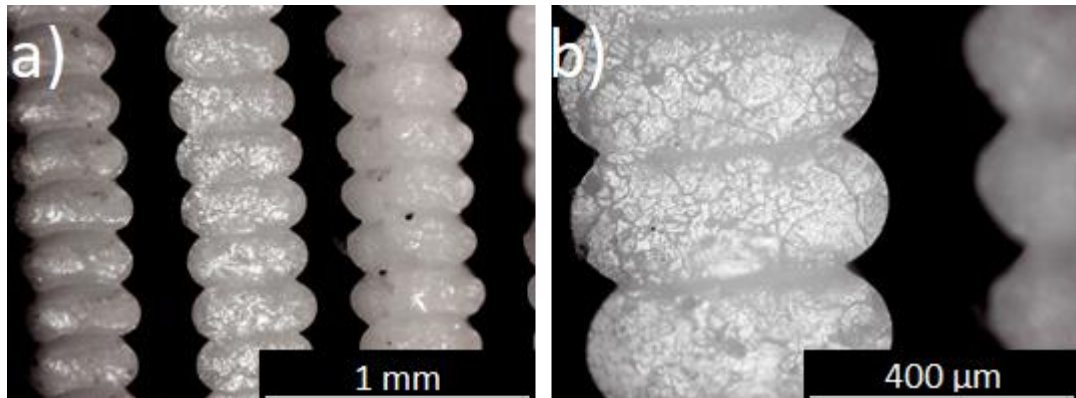


Figure 33 Micrographs of 60 percent infill printed specimen. Left micrograph shows 40x and right micrograph shows 100x magnification. The micrograph is taken from the fracture site.

60 percent infill's fracture site shows brittle nature of PLA. The crevices between the fused layers, from the Figure 3.22, can be interpreted as the minor dimple formations. The layers are fused homogeneously, and their formation held its integrity after fracture. It shows the sound of the printing as there is no delaminated layer found both by visual inspection and both by micrographs.

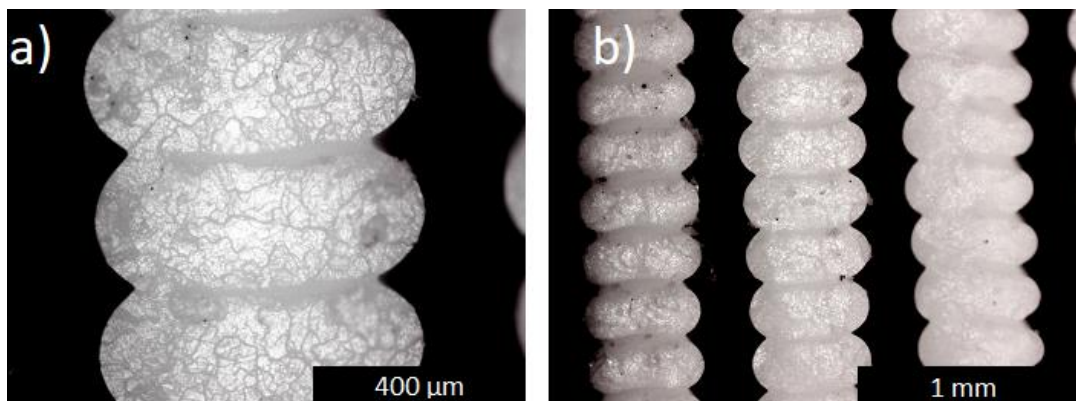


Figure 34 Micrographs of 60 percent infill printed heat treated specimen. Left micrograph shows 40x and right micrograph shows 100x magnification. The micrograph is taken from the fracture site.

The 60 percent infill and heat-treated specimen's fracture site shows the same results with the non-treated sample, in terms of micro graphical examination. From the micrographs, it can be spotted that the heat treatment did not affect the structural integrity of the specimen. This can be also validated from the mechanical data of the specimens, as the Figure 3.14. shows the increase of force resisted on tensile test conditions, after the annealing operation.

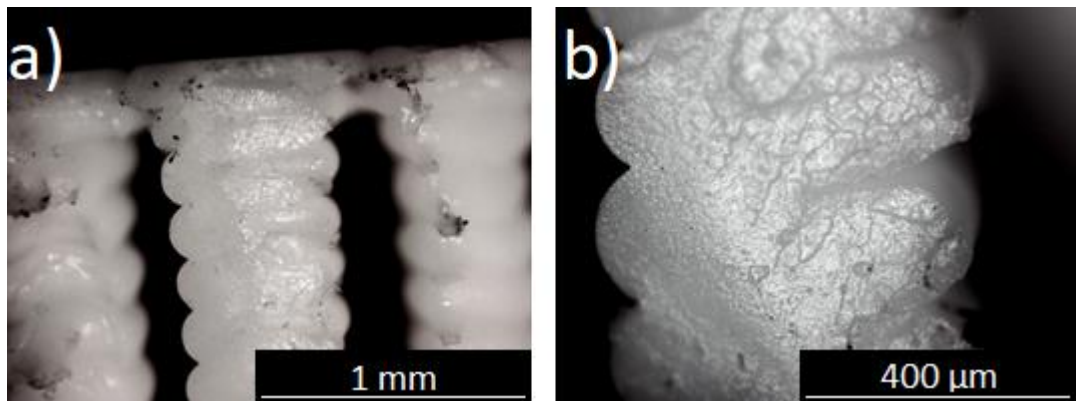


Figure 35 Micrographs of 70 percent infill printed specimen. Left micrograph shows 40x and right micrograph shows 100x magnification. The micrograph is taken from the fracture site.

The 70 percent infill printed specimen's fracture site can be seen from the Figure 3.24. Micrograph shows resemblance to 60 percent infill, yet the failure of first yielding from the fuse site then the following brittle fracture can be seen at the figure, as the shearing is evident. The printing is done homogenously with the layers stacked each other without any artifacts in between layers.

The 70 percent infill printed heat treated specimen's micrographs can be seen from the Figure 3.25. The fracture shows a brittle characteristic, which is typical to PLA's physical properties. Micrographs shows the printing results, which show no artifacts or potential weaknesses along the specimen. If the micrographs compared to the non-heat-treated 70 percent infill specimen's, Figure 3.25. has more brittle characteristic in terms of fracture, due to the smooth and clean fracture site, with no visible topography change.

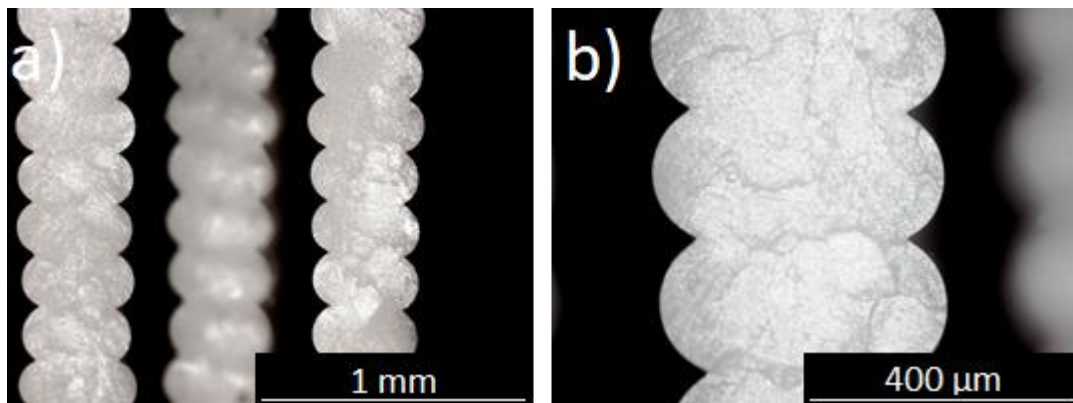


Figure 36 Micrographs of 70 percent infill printed heat treated specimen. Left micrograph shows 40x and right micrograph shows 100x magnification. The micrograph is taken from the fracture site.

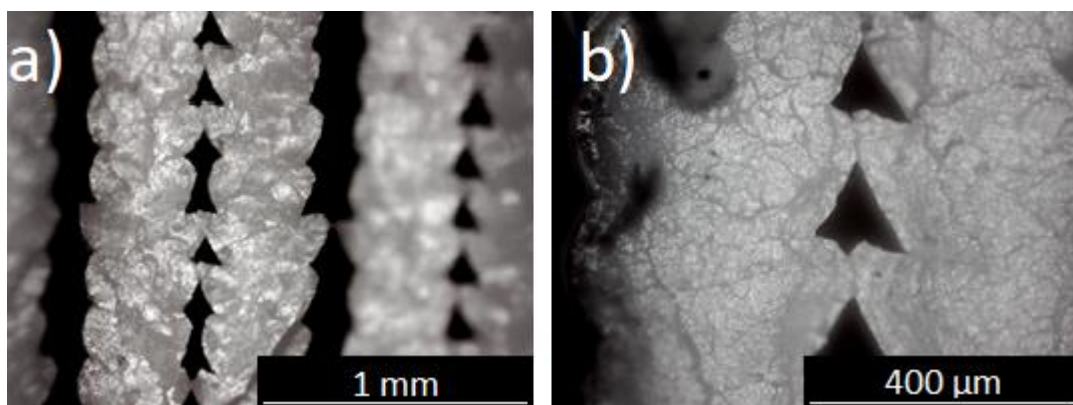


Figure 37 Micrographs of 80 percent infill printed specimen. Left micrograph shows 40x and right micrograph shows 100x magnification. The micrograph is taken from the fracture site.

80 percent infill printed specimens' micrographs can be seen from Figure 3.26. The higher infill ratio resulted in twinning of each layer to the adjacent one, due to the lower interlayer spacing. The twinned layers have an irregular bonding each other. Also, the distorted geometry along the printed layers, especially between the twinned layers can be seen from Figure 3.26. The fracture site shows the brittle fracture behaviour, as the fracture surface is clean, smooth and no visible topography change can be spotted over the fractured surface.

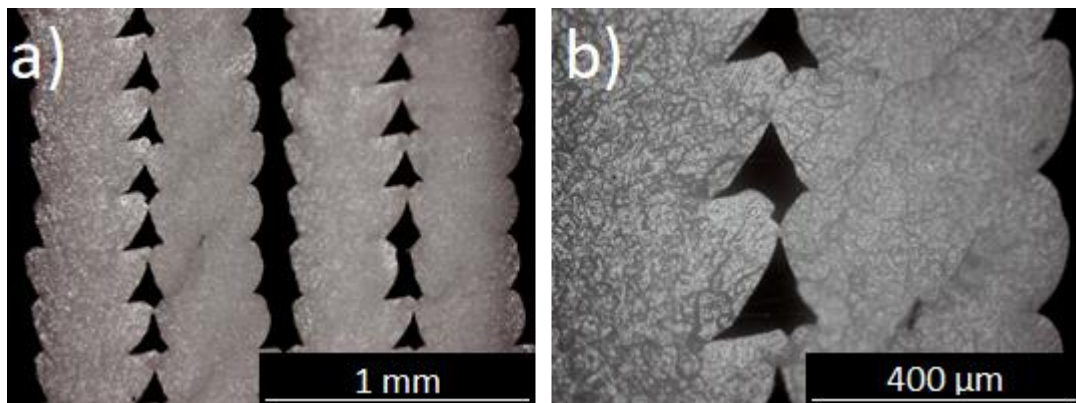


Figure 38 Micrographs of 80 percent infill printed heat treated specimen. Left micrograph shows 40x and right micrograph shows 100x magnification. The micrograph is taken from the fracture site.

80 percent infill printed heat treated specimen group's fracture site can be seen from Figure 3.27. The same geometry can be seen from the micrographs, if it is compared to the Figure 3.26. The fracture site shows brittle fracture, with a flat and smooth surface, and the printing shows no artifacts aside of the randomly unfused parts at the twinned layers.

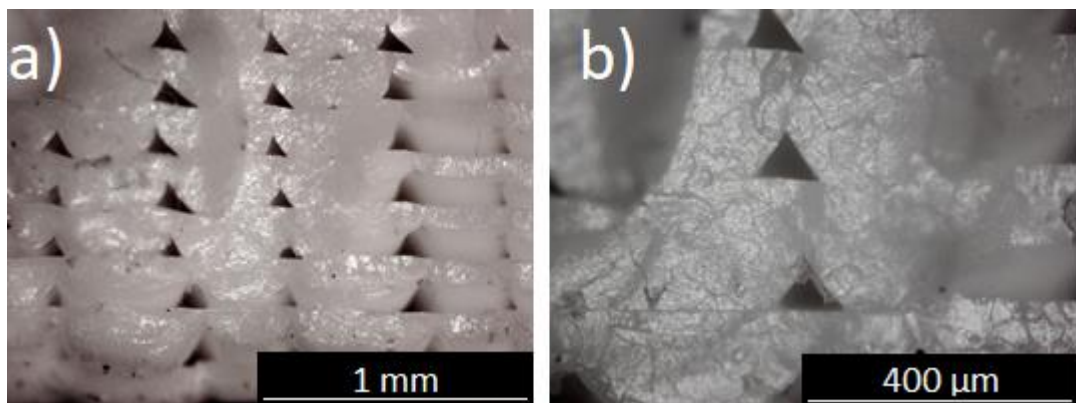


Figure 39 Micrographs of 90 percent infill printed specimen. Left micrograph shows 40x and right micrograph shows 100x magnification. The micrograph is taken from the fracture site.

90 percent infill printed specimen group's fracture site can be seen at Figure 3.28

The layers are stacked tighter and instead of twinning, all the layers are fused to each other, both in vertical and horizontal axis. Due to fusion between each neighbouring layer, the shape of the layers is in a semi-circular shape with a triangular gap between each neighbouring layer. There is no artifacts found during the inspection of the micrographs and materials itself.

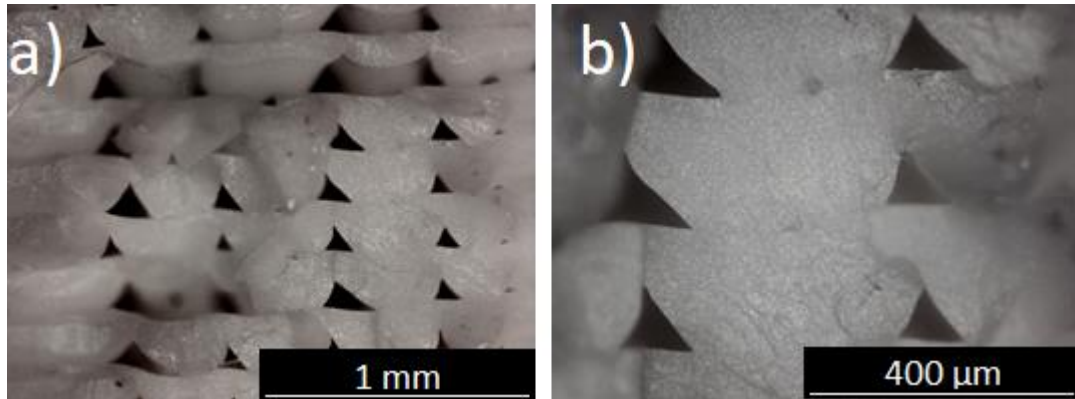


Figure 40 Micrographs of 90 percent infill printed heat treated specimen. Left micrograph shows 40x and right micrograph shows 100x magnification. The micrograph is taken from the fracture site.

90 percent infill printed heat treated group's fracture site can be seen at Figure 3.29. There is no structural difference between the heat treated and non treated one, as the heat treatment shows no distortion of the structure. Fracture site shows the brittle failure type. Note the brighter and smoother surface of the fracture site, as it hints the heat treatment decreased the ductility of the material.

100 percent infill printed specimen group's micrographs can be seen at Figure 3.30. The same structure from 90 percent is being preserved and the triangular voids between each neighbouring layers are smaller and more homogenous than the former one. The fusion between layers has no unexpected or unwanted voids or artifacts. The micrograph shows the printing is done without any error, as the printed beads are stacked homogeneously and with no disorder. The layers show homogenous widths and heights, and the printing is done as the same it is shown in

the slicer program (Ultimaker Cura).

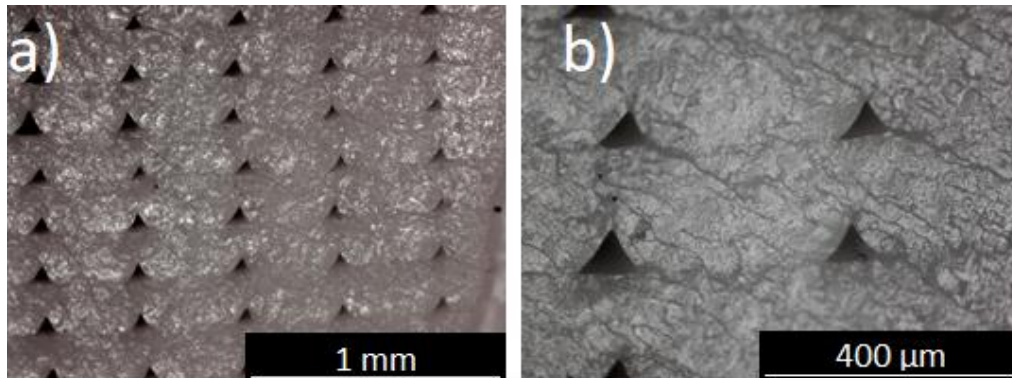


Figure 41 Micrographs of 100 percent infill printed specimen. Left micrograph shows 40x and right micrograph shows 100x magnification. The micrograph is taken from the fracture site.

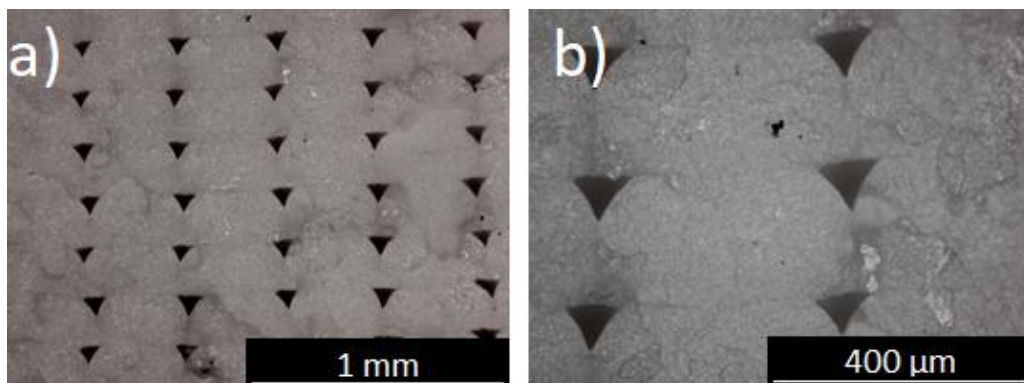


Figure 42 Micrographs of 100 percent infill printed heat treated specimen. Left micrograph shows 40x and right micrograph shows 100x magnification. The micrograph is taken from the fracture site.

100 percent infill printed heat treated specimen group's micrographs can be seen at Figure 3.31. No structural difference can be spotted between the treated and to the non-treated sample group. There is no compromise of fusion or stacking behaviour and treatment did not alter the print structure. The fracture zone shows clear signs of brittle fracture and the fracture surface is smoother than the non-heat treated sample, showing the brittle nature of the treated sample.

CHAPTER 4

CONCLUSION AND FUTURE WORK

Fused filament fabrication is a widely used technology, especially to print thermoplastics. Polylactide is one of the most widely used filaments in the market. Availability, bio-compatibility and ease to print and use are the main factors to increase its appeal in the market.

It is known that different crystal morphologies can be introduced to polylactide via heat treatment method. This post-production treatment is tested with conventional production methods. Yet the heat treatment of fused filament fabricated polylactide specimens are not analysed extensively. This work aimed to alter the properties of fused filament fabricated polylactide specimens.

It is found that the two different crystalline phases of α and α' , are incepted into the material, by heat treatment procedures. Phase transformation from α' to α is found at 100 °C. This can be both seen by DSC graphs and XRD data. In DSC, the characteristic endotherms can be seen after this transformation. In XRD data, the drastic shift on peaks and rapid expansion, then the shrinkage of the volume of crystalline phases.

The formation of α and α' and their coexistence are revalidated by experiments and values similar to literature values are shown. It is concluded that the polylactide filament used is not the pure polylactide yet the impurities did not change the behaviour greatly.

Heat treatment also causes shrinkage, on the samples, as it is both seen in SEM pictures and calculated crystalline volume. The crystalline volumes are calculated by using XRD data and Bragg's law and showed a trend of reduction along the increased trend of treatment temperatures. SEM pictures show the differences

between the treated samples. It is found that the increased temperature of the treatment, also introduces gaps along the printed layers. This is due to the increased density, which is shown in the works of literature.

It is concluded that, the expansion and shrinkage of the crystals, and the thermal shock combined from the printing procedure deteriorates the specimens. Literature data shows that the inception of crystalline phases increase the mechanical properties, yet the research data shows the rapid deterioration after 100 °C treatment. This can be tied to the crystal size behaviour, as the shrinkage-expansion-shrinkage trend is noted along the increased annealing temperatures.

It has been also shown in the literature, that inclusion of crystals via heat treatment is beneficial for tensile stress values. However due to the porous structure of printed specimens, the shrinkage-expansion-shrinkage cycle would perform differently than in mold injected specimens. Since the porous structure would mean there would be voids all along the material, the density changes may mean microcracks, or deformations at the edges of the voids and pores. That can be the reason of the rapid deterioration of the post 100 °C annealing temperatures. These microcracks cant be seen via SEM, unfortunately, as the zooming capabilities are limited on usage of polylactide. The reason is the heating and melting of the material, as the zooming would mean more electrons are focused into a smaller space, increasing the specimen's temperature, leading to melting of the surface. This has been tried and the damaged specimen is discarded.

The best mechanical test results are displayed by S100 group. The heat treatment showed an improvement for stress value of 6,5 % and strain value of 33,5 %. It can be said that the most beneficial heat treatment is done by 100 °C and α' crystals benefitted most for the printed specimens.

The elastic modulus values are improved gradually by inclusion of heat treatment. Compared to the reference sample, S100 group has 12,3 % improvement, and S140 has 26,0 % improvement as maximum improvement.

For the infill-controlled group, best tensile strength is achieved by 100% infill printed and tempered specimen. This is expected as it is the specimen group which has the most layers printed in the same volume.

Best tensile strength per printed layer is achieved by 60% infill printed and tempered specimen. As it is known from the first stage experiments, that the stress improvement is expected, yet it was expected that all groups would show the same strength per printed layer ratio. Reason for this result is due to the printed structure of the specimen. The prints of 50-60-70 percent infill specimens showed that the independent layers with only fused at Y direction, yet 80 percent infill showed the twinned layers, with only the duo of layers stacked each other at X direction, and 90-100 percent infill printed ones showed the fusion at both X and Y direction between the layers. The strength per layer data shows that the most effective structure is the independent layers, which are only fused at Y direction. The best resilience per layer is also achieved by 60% infill printing.

Best strain at breakage is achieved by 60% infill printed specimen. This can be validated by inspecting the micrographs. The micrographs show the slight dimple formation at the fused sites and comparatively irregular surface shows the signs of more ductile behaviour of the material. This kind of behaviour can be explained with more homogenous structure, less edges, which can result in less stress concentration factor. The second factor can be the lower number of fusion sites. The fusion sites can deteriorate the material's strength as they initiate a heat affected zone to the neighbouring and already printed layer.

The average tensile stress improvement via tempering is 7.3 % for infill-controlled specimens. The improvement for 60% infill is 9.0% and for 70% infill is 10.1%. It has been found that the tempering results reduction of strain for every specimen. While 60% and 70% infill printed specimens show resilience increase after tempering, the other specimens show decrease in resilience values.

4.1 Future Work

These property changes can be and still used in the industry. Heat treatment of steels are widespread and used in full effect. Same effects are also applied on the polylactide, as it is found that the mechanical properties are improved by employing heat treatment over the printed specimens. An engineer can use those data for improving different aspects. For example, improvement of elastic modulus can be used as a shock absorbent property, which can be used on different applications, from footwear to ballistic materials. If the focus is narrowed down from polymers to the polylactide materials produced by additive manufacturing, it is known that polylactide is used in different biomedical applications. These findings can be beneficial to tailoring the porous structure of a bio scaffold, increasing its mechanical properties, which would enhance in return, the experience of end user. There have been researches amongst the literature about the bio properties of polylactide which are compared to the crystallinity ratios. Merging the data extracted from this or similar research can be used to tailor a product further, according to the demands of the user or medium.

The unintended effect of shrinkages and density changes can lead into porosity size changes. The porosity size alterations can provide useful on different applications. There can be a plethora of applications by employing the density changes. One of the first application that comes into the mind is the inclusion of microporosities. Hypothetically, very small features or pores alongside the layers, can be introduced, since the density change is intrinsic. A macro feature can be increased furthermore with more temperature-sensitive materials, be it polymer, metal, or ceramic. More temperature resistant materials which can introduce phase changes with differing density phases, can be a more ideal material for creating of intrinsically tailored pores or features. Though this density change would be only useful if there is already a crafted pore along the material, as the change of phases cannot create pores itself. In addition, the density changes would be percentage based, which can be concluded that the pore size would be changed in percentages.

There are potential usages, as it is known that there are nanosized porous materials such as zeolite, graphene, or platinum. Any kind of incremental change can create difference for such features. Yet if it is focused with the additive manufacturing process, the manufacturing processes with higher resolution, can benefit more from the pore size changes. This pore tailoring can be thought inversely either. The material's crystallinity can be decreased, hence creating smaller pores in return. This can lead to the production of a smaller sized pores, which are introduced via additive manufacturing beforehand.

Alongside with the pore size, density changes along the material due to phase transformation, can increase the surface roughness along the pores, if the material is constrained to not to change its shape. Any solid-to-solid phase transformation can be a candidate for this and can have uses along industry. It is known that rough surfaces and porosity is a desired property for biomedical applications. A future work focused on biomedical applications and surface roughness which would use additive manufacturing and heat treatment in tandem, is feasible.

Different materials, especially metals can be selected to be another candidate material for future work. Removal or reduction of gaps without melting the material can be a beneficial, future prospect for research, especially removing gaps on SLS printed metals can be a huge boon. Another future prospect can be improvement of medical crafts that are produced by additive manufacturing, by employing heat treatment and inclusion of crystallinity, and with different pore structures, architectures, and pore shapes. Not limited to medical industry, this behaviour can be tested on the epoxy-based composites, as the density change may create beneficial results on adhesion of matrix.

Same research can be repeated, by using a fully filled, non-porous printed structure, and compared to an injection moulded group. This would require a custom code to fully fill the gaps of previous layers to produce a full infill. The new layer must compensate the previous layer's gaps, hence producing a non-porous structure.

REFERENCES

- Almeida, G. (2020). *Diccionario Kuttercraft*.
<https://www.kuttercraft.com/post/diccionario-kuttercraft>
- Alssabbagh, M., Tajuddin, A. A., Abdulmanap, M., & Zainon, R. (2017). Evaluation of 3D printing materials for fabrication of a novel multi-functional 3D thyroid phantom for medical dosimetry and image quality, *Radiat. Phys. Chem*, 135, 106–112.
<https://doi.org/10.1016/j.radphyschem.2017.02.009>.
- Anderoglu, O. (2004). *Residual Stress Measurement Using X-Ray Diffraction*.
- Auras, R., Harte, B., & Selke, S. (2004). An Overview of Polylactides as Packaging Materials. *Macromolecular Bioscience*, 4(9), 835–864.
<https://doi.org/10.1002/mabi.200400043>
- Averback, R. S., & Rubia, T. D. (1997). *Displacement Damage in Irradiated Metals and Semiconductors*.
- Barkhad, M. S., Abu-Jdayil, B., Mourad, A. H. I., & Iqbal, M. Z. (2020). Thermal Insulation and Mechanical Properties of Polylactic Acid (PLA) at Different Processing Conditions. *Polymers*, 12(9), 2091.
<https://doi.org/10.3390/polym12092091>
- Behzadnasab, M., & Yousefi, A. (2016). *Effects of 3D printer nozzle head temperature on the physical and mechanical properties of PLA based product*.

- Booth, A., Kubowicz, S., Beegle-Krause, C., Skancke, J., Nordam, T., Landsem, E., Throne-Holst, M., & Jahren, S. (2017). In *M-918/2017-Unrestricted Report Microplastic in global and Norwegian marine environments: Distributions, degradation mechanisms and transport author(s)*.
- Bragg W.H., Bragg W.L., The reflection of X-rays by crystals. (1913). *Proceedings of the Royal Society of London. Series A, Containing Papers of a Mathematical and Physical Character*, 88(605), 428–438.
<https://doi.org/10.1098/rspa.1913.0040>
- Brizzolara, D., Cantow, H.-J., Diederichs, K., Keller, E., & Domb, A. M. (1982.).
- Broz, M. (2003). Structure and mechanical properties of poly(?,?-lactic acid)/poly(ϵ -caprolactone) blends. *Biomaterials*, 24(23), 4181–4190.
[https://doi.org/10.1016/S0142-9612\(03\)00314-4](https://doi.org/10.1016/S0142-9612(03)00314-4)
- Carrasco, F., Pagès, P., Gámez-Pérez, J., Santana, O. O., & MasPOCH, M. L. (2010). Processing of poly(lactic acid): Characterization of chemical structure, thermal stability and mechanical properties. *Polym. Degrad. Stab*, 95, 116–125. <https://doi.org/10.1016/j.polymdegradstab.2009.11.045>.
- Cebe, P., & Hong, S.-D. (1986). Crystallization behaviour of poly(ether-ether-ketone). *Polymer*, 27(8), 1183–1192. [https://doi.org/10.1016/0032-3861\(86\)90006-6](https://doi.org/10.1016/0032-3861(86)90006-6)
- Committee, D. (XXXX). Test Method for Tensile Properties of Plastics. *ASTM International*. <https://doi.org/10.1520/D0638-14>.
- Doumeng, M., Makhlouf, L., Berthet, F., Marsan, O., Delbé, K., Denape, J., & Chabert, F. (2021). A comparative study of the crystallinity of

polyetheretherketone by using density, DSC, XRD, and Raman spectroscopy techniques. *Polymer Testing*, 93, 106878.

<https://doi.org/10.1016/j.polymertesting.2020.106878>

Farah, S., Anderson, D. G., & Langer, R. (2016). Physical and mechanical properties of PLA, and their functions in widespread applications—A comprehensive review, *Adv. Drug Deliv. Rev.*, 107, 367–392.

<https://doi.org/10.1016/j.addr.2016.06.012>.

Foglia, F., De Meo, A., Iozzino, V., Volpe, V., & Pantani, R. (2020). Isothermal crystallization of PLA: Nucleation density and growth rates of α and α' phases. *The Canadian Journal of Chemical Engineering*, 98(9), 1998–2007.

<https://doi.org/10.1002/cjce.23818>

Garlotta, D. (2001). A Literature Review of Poly(Lactic Acid). *J. Polym. Environ.*, 9, 63–84. <https://doi.org/10.1023/A:1020200822435>.

Gupta, M. C., & Deshmukh, V. G. (1982). Thermal oxidative degradation of polylactic acid. *Colloid Polym. Sci.*, 260, 308–311.

<https://doi.org/10.1007/BF01447969>.

Gurrapu, S. (2020). *Make desktop 3D printing more affordable with DLP® PICOTM technology. DLP technology—Technical articles—TI E2E support forums.* https://e2e.ti.com/blogs_/b/enlightened/posts/making-new-desktop-3d-printing-applications-possible-and-more-affordable-with-dlp-pico-technology

Henry, B. W., & Lawrence, B. W. (n.d.). The reflection of X-rays by crystals *Proc. R. Soc. Lond. A.* <https://doi.org/10.1098/rspa.1913.0040>

- Holdsworth, P. J., & Turner-Jones, A. (1971). The melting behaviour of heat crystallized poly(ethylene terephthalate). *Polymer*, *12*(3), 195–208. [https://doi.org/10.1016/0032-3861\(71\)90045-0](https://doi.org/10.1016/0032-3861(71)90045-0)
- Huang, C.-I., Tsai, S.-H., & Chen, C.-M. (2006). Isothermal crystallization behavior of poly(L-lactide) in poly(L-lactide)-block-poly(ethylene glycol) diblock copolymers. *Journal of Polymer Science Part B: Polymer Physics*, *44*(17), 2438–2448. <https://doi.org/10.1002/polb.20890>
- Iannace, S., & Nicolais, L. (1997). Isothermal crystallization and chain mobility of poly(L-lactide). *Journal of Applied Polymer Science*, *64*(5), 911–919. [https://doi.org/10.1002/\(sici\)1097-4628\(19970502\)64:5](https://doi.org/10.1002/(sici)1097-4628(19970502)64:5)
- Intertek. (2021.). *Heat of Fusion / Crystallization / Melting Point / Glass Transition by DSC (Differential Scanning Calorimeter)*. <https://www.ptli.com/testlopedia/tests/DSC-d3417.asp>
- Kawai, T., Rahman, N., Matsuba, G., Nishida, K., Kanaya, T., Nakano, M., Okamoto, H., Kawada, J., Usuki, A., Honma, N., Nakajima, K., & Matsuda, M. (2007). Crystallization and Melting Behavior of Poly (L -lactic Acid). *Macromolecules*, *40*(26), 9463–9469. <https://doi.org/10.1021/ma070082c>
- Kaygusuz, B., & Özerinç, S. (2019). Improving the Ductility of Polylactic Acid Parts Produced by Fused Deposition Modeling through Polyhydroxyalkanoate Additions. *Journal of Applied Polymer Science*, *136*(43), 48154. <https://doi.org/10.1002/app.48154>.
- Lamba, D. (2016). Wide-Angle X-Ray Diffraction Pattern. *Encyclopedia of Membranes*. https://doi.org/10.1007/978-3-662-44324-8_1099

- Lisa SLS 3d printer - Sinterit - manufacturer of high Quality SIs 3D printers.
Sinterit. (2021, June 11). Retrieved September 28, 2021, from
<https://www.sinterit.com/sinterit-lisa/>.
- Marubayashi, H., Akaishi, S., Akasaka, S., Asai, S., & Sumita, M. (2008).
Crystalline Structure and Morphology of Poly(L -lactide) Formed under
High-Pressure CO₂. *Macromolecules*, 41(23), 9192–9203.
<https://doi.org/10.1021/ma800766h>
- Maspoch, M. L., Gamez-Perez, J., Gimenez, E., Santana, O. O., & Gordillo, A.
(2004). Influence of processing on ethylene-propylene block copolymers:
Structure and mechanical behavior. *Journal of Applied Polymer Science*,
93(6), 2866–2878. <https://doi.org/10.1002/app.20834>
- MATEOS-TIMONEDA, M. A. (2009). Polymers for bone repair. *Bone Repair
Biomaterials*, 231–251. <https://doi.org/10.1533/9781845696610.2.231>
- Matbase. (2012).
<https://web.archive.org/web/20120210194852/http://www.matbase.com/material/polymers/agrobased/polylactic-acid-pla/properties>
- Mckeen. (n.d.). *L.,The Effect of Sterilization on Plastics and Elastomers (Third
Edition),William Andrew Publishing,2012,Pages 57-84,ISBN
781455725984,https://doi.org/10.1016/B978-1-4557-2598-4.00003-4.*
- Mohamed, O. A., Masood, S. H., & Bhowmik, J. L. (2015). Optimization of fused
deposition modeling process parameters: A review of current research and
future prospects. *Advances in Manufacturing*, 3(1), 42–53.
<https://doi.org/10.1007/s40436-014-0097-7>

- Odell, D., Wright, P. K., Montero, M., Roundy, S., & Ahn, S. (2002). Anisotropic material properties of fused deposition modeling ABS, *Rapid Prototyp. J*, 8, 248–257. <https://doi.org/10.1108/13552540210441166>.
- Pan, P., Zhu, B., Kai, W., Dong, T., & Inoue, Y. (2008a). Effect of crystallization temperature on crystal modifications and crystallization kinetics of poly(L-lactide). *Journal of Applied Polymer Science*, 107(1), 54–62. <https://doi.org/10.1002/app.27102>
- Pan, P., Zhu, B., Kai, W., Dong, T., & Inoue, Y. (2008b). Polymorphic Transition in Disordered Poly(L-lactide) Crystals Induced by Annealing at Elevated Temperatures. *Macromolecules*, 41(12), 4296–4304. <https://doi.org/10.1021/ma800343g>
- Rasal, R. M., Janorkar, A. V., & Hirt, D. E. (2010). Poly(lactic acid) modifications, *Prog. Polym. Sci*, 35, 338–356. <https://doi.org/10.1016/j.progpolymsci.2009.12.003>.
- Rasselet, D., Ruellan, A., Guinault, A., Miquelard-Garnier, G., Sollogoub, C., & Fayolle, B. (2014). Oxidative degradation of polylactide (PLA) and its effects on physical and mechanical properties. *European Polymer Journal*, 50, 109–116. <https://doi.org/10.1016/j.eurpolymj.2013.10.011>
- Rebelo, R., Vila, N., Rana, S., & Fangueiro, R. (2016). Poly Lactic Acid Fibre Based Biodegradable Stents and Their Functionalization Techniques. In *Natural Fibres: Advances in Science and Technology Towards Industrial Applications* (pp. 331–342). https://doi.org/10.1007/978-94-017-7515-1_25.

- Senatov, F. S., Niaza, K. V., Zadorozhnyy, M. Y., Maksimkin, A. V., Kaloshkin, S. D., & Estrin, Y. Z. (2016). Mechanical properties and shape memory effect of 3D-printed PLA-based porous scaffolds. *J. Mech. Behav. Biomed. Mater*, 57, 139–148. <https://doi.org/10.1016/j.jmbbm.2015.11.036>.
- Srithep, Y., Pholharn, D., & Morris, J. (2019). Injection-molded poly(L-lactic acid)/poly(D-lactic acid) blends: Thermal and mechanical properties. 030019. <https://doi.org/10.1063/1.5088277>
- Sood, A. K., Ohdar, R. K., & Mahapatra, S. S. (2010). Parametric appraisal of mechanical property of fused deposition modelling processed parts, *Mater. Des*, 31, 287–295. <https://doi.org/10.1016/j.matdes.2009.06.016>.
- Tábi, T., Hajba, S., & Kovács, J. G. (2016). Effect of crystalline forms (α' and α) of poly(lactic acid) on its mechanical, thermo-mechanical, heat deflection temperature and creep properties. *European Polymer Journal*, 82, 232–243. <https://doi.org/10.1016/j.eurpolymj.2016.07.024>
- Tabi, T., Sajo, I. E., Szabo, F., Luyt, A. S., & Kovacs, J. G. (2010). Crystalline structure of annealed polylactic acid and its relation to processing. *Express Polymer Letters*, 4(10), 659–668. <https://doi.org/10.3144/expresspolymlett.2010.80>
- Tang, Z., Zhang, C., Liu, X., & Zhu, J. (2012). The crystallization behavior and mechanical properties of polylactic acid in the presence of a crystal nucleating agent. *J. Appl. Polym. Sci*, 125, 1108–1115. <https://doi.org/10.1002/app.34799>.

- Tanikella, N. G., Wittbrodt, B., & Pearce, J. M. (2017). Tensile strength of commercial polymer materials for fused filament fabrication 3D printing, *Addit. Manuf*, *15*, 40–47. <https://doi.org/10.1016/j.addma.2017.03.005>.
- Tsuji, H., Takai, H., & Saha, S. K. (2006). Isothermal and non-isothermal crystallization behavior of poly(l-lactic acid): Effects of stereocomplex as nucleating agent. *Polymer*, *47*(11), 3826–3837. <https://doi.org/10.1016/j.polymer.2006.03.074>
- Tymrak, B. M., Kreiger, M., & Pearce, J. M. (2014). Mechanical properties of components fabricated with open-source 3-D printers under realistic environmental conditions, *Mater. Des*, *58*, 242–246. <https://doi.org/10.1016/j.matdes.2014.02.038>.
- Valerga, A., Batista, M., Salguero, J., & Girot, F. (2018). Influence of PLA Filament Conditions on Characteristics of FDM Parts. *Materials*, *11*(8), 1322. <https://doi.org/10.3390/ma11081322>
- Wen, L., & Xin, Z. (2010). Effect of a Novel Nucleating Agent on Isothermal Crystallization of Poly(L-lactic acid). *Chinese Journal of Chemical Engineering*, *18*(6), 899–904. [https://doi.org/10.1016/S1004-9541\(09\)60145-2](https://doi.org/10.1016/S1004-9541(09)60145-2)
- Wong, K. V., & Hernandez, A. (2012). A Review of Additive Manufacturing, *Int. Sch. Res. Not*. <https://doi.org/10.5402/2012/208760>.
- Yao, T., Deng, Z., Zhang, K., & Li, S. (2019). A method to predict the ultimate tensile strength of 3D printing polylactic acid (PLA) materials with

- different printing orientations. *Composites Part B: Engineering*, 163, 393–402. <https://doi.org/10.1016/j.compositesb.2019.01.025>
- Yu, L., Liu, H., Xie, F., Chen, L., & Li, X. (2008). Effect of annealing and orientation on microstructures and mechanical properties of polylactic acid. *Polym. Eng. Sci*, 48, 634–641. <https://doi.org/10.1002/pen.20970>.
- Zhao, L., Jiang, Z., Zhang, C., & Jiang, Z. (2021). Development model and experimental characterization of residual stress of 3D printing PLA parts with porous structure. *Applied Physics A*, 127(2), 98. <https://doi.org/10.1007/s00339-020-04238-2>
- Zhong, W., Li, F., Zhang, Z., Song, L., & Li, Z. (2001). Short fiber reinforced composites for fused deposition modeling, *Mater. Sci. Eng. A*, 301, 125–130. [https://doi.org/10.1016/S0921-5093\(00\)01810-4](https://doi.org/10.1016/S0921-5093(00)01810-4).
- Zhou, W. Y., Duan, B., Wang, M., & Cheung, W. L. (2009). Crystallization kinetics of poly(L-lactide)/carbonated hydroxyapatite nanocomposite microspheres. *Journal of Applied Polymer Science*, 113(6), 4100–4115. <https://doi.org/10.1002/app.30527>